Supporting Information

Simple Molecular Ferroelectrics: *N*,*N*'-Dialkyl-terephthalamide Derivatives in Solid Phase

Moeko Kawana,[a] Ryohei Mizoue,[a] Takashi Takeda,[a, b]* Norihisa Hoshino,[a, b] and Tomoyuki Akutagawa [a, b, c]*

[a] Graduate School of Engineering, Tohoku University, Sendai 980-8579, Japan.

[b] Institute of Multidisciplinary Research for Advanced Materials (IMRAM), Tohoku University, 2-1-1 Katahira, Aoba-ku, Sendai 980-8577, Japan.

[c] National Institute for Material Science (NIMS), 1-2-1 Tsukuba, 305-0047, Japan

Institute of Multidisciplinary Research for Advanced Materials (IMRAM), Tohoku University, 2-1-1 Katahira, Aoba-ku, Sendai 980-8577, Japan

Phone: +81-22-217-5653

Fax: +81-22-217-5655

E-mail akutagawa@tohoku.ac.jp and takashi@tohoku.ac.jp

Contents

Experimental

Preparations of CnTPAs. All the **CnTPA** derivatives were prepared by the condensation reaction between terephthaloyl dichloride (50 mmol) and the corresponding $C_nH_{2n+1}NH_2$ (13 mmol) with n = 5−16, 18 in anhydrous THF (35 mL) in the presence of Et_3N (18 mmol). The reaction mixture was stirred at 298 K for 24 h, and the white precipitate was collected by filtration. The white powder was recrystallized 2–4 times from toluene:isopropanol (v/v = 1:1).

N,*N*'-Diamyl-1,4-terephthalamide (**C5TPA**). Yield = 62 %, elemental analysis. Calc. for $C_{18}H_{28}N_2O_2$: C, 70.78; H, 9.27; O, 9.20; N, 10.51. Found: C, 70.78; H, 9.31; N, 9.16. ^{1}H NMR ($CDCl_3$, 400 MHz, δ in ppm) 0.88 (6H, t, J=7.1 Hz, -CH_3), 1.35–1.40 (8H, m, -CH_2-), 1.64 (4H, quin, J=7.3 Hz, -NH-CH_2-CH_2-), 3.47 (4H, q, J=6.8 Hz, -NH-CH_2-), 6.12 (2H, t, J=4.0 Hz, -NH-), 7.81 (4H, s, Benzene). HRMS (FAB) calc. for $C_{18}H_{29}O_2H_2$: 305.2229 [$(M^+H)^+$]. Found: 305.2233.

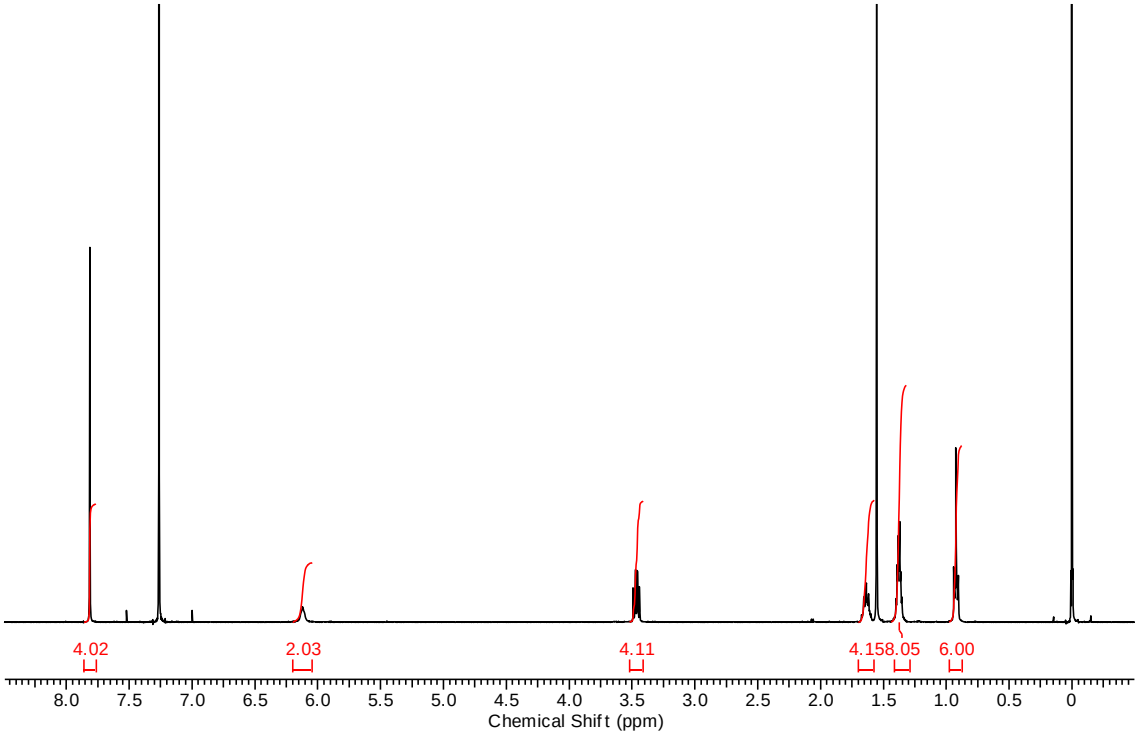

^{1}H NMR spectrum of **C5TPA** in $CDCl_3$.

N,*N*'-Dihexyl-1,4-terephthalamide (**C6TPA**) Elemental analysis. Calc. for $C_{20}H_{32}N_2O_2$: C, 72.25; H, 9.70; N, 8.41. Found: C, 72.01; H, 9.67; N, 8.41. $_1$H NMR ($CDCl_3$, 400 MHz, δ in ppm) 0.90 (6H, t, J=7.0 Hz, -CH_3), 1.31–1.41 (12H, m, -CH_2-), 1.63 (4H, quin, J=7.3 Hz, -NH-CH_2-CH_2-),

3.47 (4H, q, *J*=6.1 Hz, -NH-CH_2-), 6.11 (2H, t, *J*=6.41 Hz, -NH-), 7.82 (4H, s, Benzene).

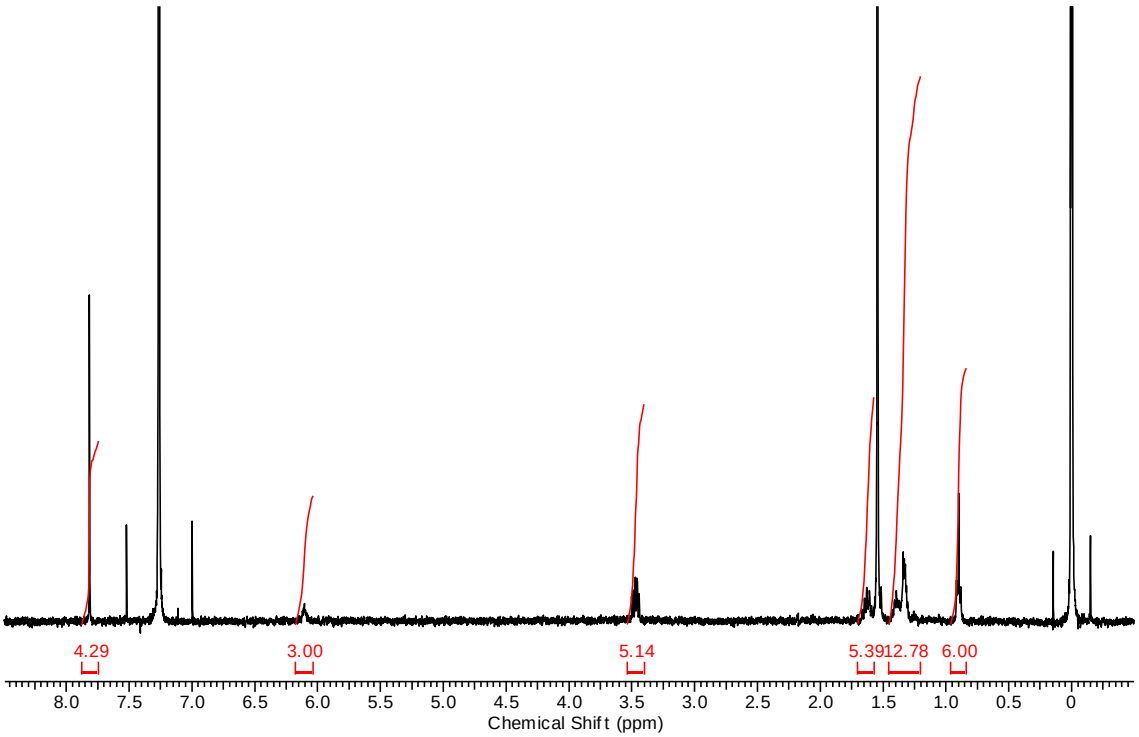

^{1}H NMR spectrum of **C6TPA** in $CDCl_3$.

N,*N*'-Diheptyl-1,4-terephthalamide (**C7TPA**). Yield = 65%. Elemental analysis. Calc. for $C_{22}H_{36}N_2O_2$: C, 73.29; H, 10.06; N, 7.77. Found: C, 73,33; H, 10.31; N, 7.77. ^{1}H NMR ($CDCl_3$, 400 MHz, δ in ppm) 0.89 (6H, t, *J*=6.3 Hz, -CH_3), 1.30–1.40 (16H, m, -CH_2-), 1.63 (4H, quin, *J*=7.0 Hz, -NH-CH_2-CH_2-), 3.46 (4H, q, *J*=6.7 Hz, -NH-CH_2-), 6.13 (2H, t, *J*=4.5 Hz, -NH-), 7.81 (4H, s, Benzene). HRMS (FAB) calc. for $C_{22}H_{37}O_2H_2$: 368.2858 [$(M^+H)^+$]. Found: 368.2855.

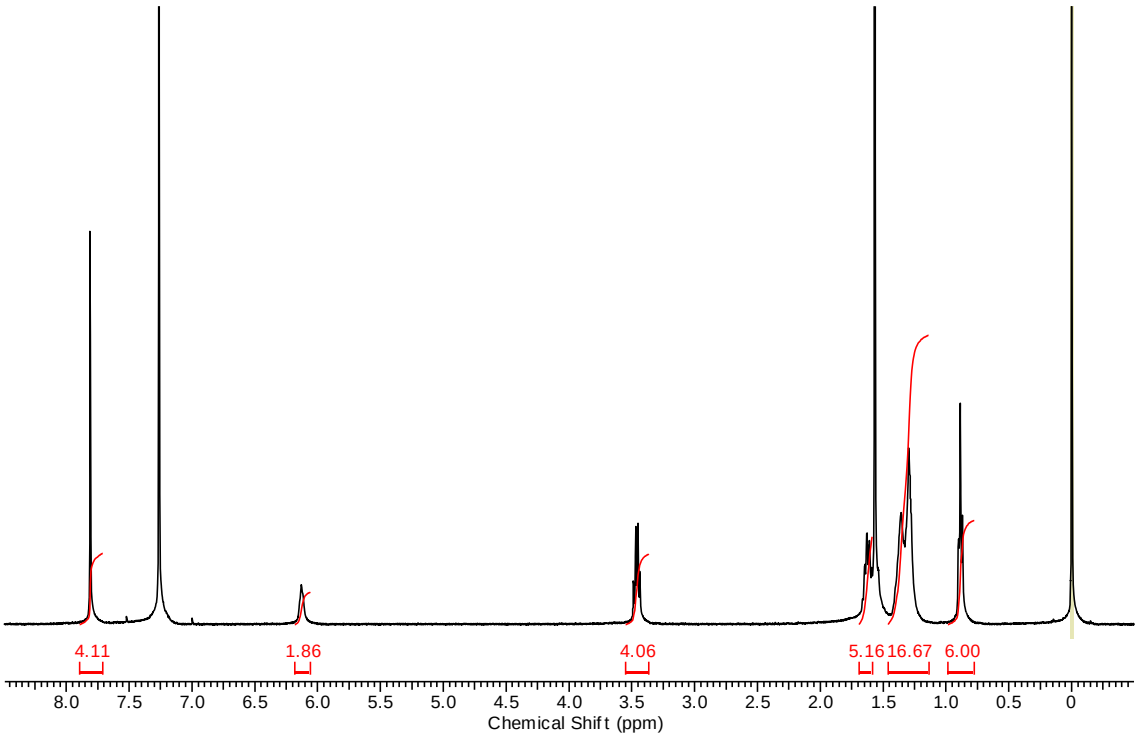

^{1}H NMR spectrum of **C7TPA** in $CDCl_3$.

N,*N*'-Dioctyl-1,4-terephthalamide (**C8TPA**) Yield = 90%. Elemental analysis. Calc. for $C_{24}H_{40}N_2O_2$: C, 74.18; H, 10.38; N, 7.21. Found: C, 74.21; H, 10.62; N, 7.20. ^{1}H NMR ($CDCl_3$, 400 MHz, δ in ppm) 0.88 (6H, t, *J*=5.0 Hz, -CH_3), 1.28–1.40 (20H, m, -CH_2-), 1.63 (4H, quin, *J*=6.5 Hz, -NH-CH_2-CH_2-), 3.47 (4H, q, *J*=5.9 Hz, -NH-CH_2-), 6.12 (2H, t, *J*=4.8 Hz, -NH-), 7.81 (4H, s, Benzene).

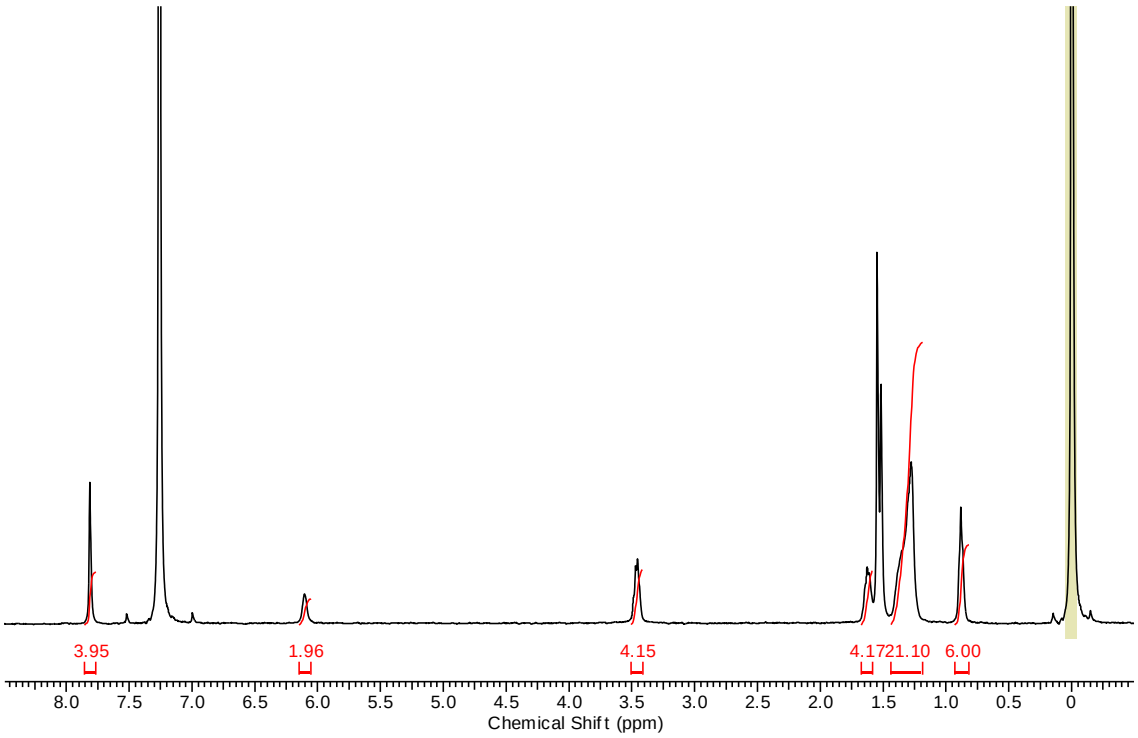

^{1}H NMR spectrum of **C8TPA** in $CDCl_3$.

N,*N*'-Dinonanyl-1,4-terephthalamide (**C9TPA**) Yield = 71%. Elemental analysis. Calc. for $C_{26}H_{44}N_2O_2$: C, 74.95; H, 10.64; N, 6.72. Found: C, 74.79; H, 10.82; N, 6.74. ^{1}H NMR ($CDCl_3$, 400 MHz, δ in ppm) 0.88 (6H, t, *J*=7.0 Hz, -CH_3), 1.27–1.40 (24H, m, -CH_2-), 1.63 (4H, quin, *J*=7.3 Hz, -NH-CH_2-CH_2-), 3.47 (4H, q, *J*=6.7 Hz, -NH-CH_2-), 6.10 (2H, t, *J*=4.6 Hz, -NH-), 7.81 (4H, s, Benzene). HRMS (FAB) calc. for $C_{26}H_{45}O_2H_2$: 417.3481 [$(M^+H)^+$]. Found: 417.3479.

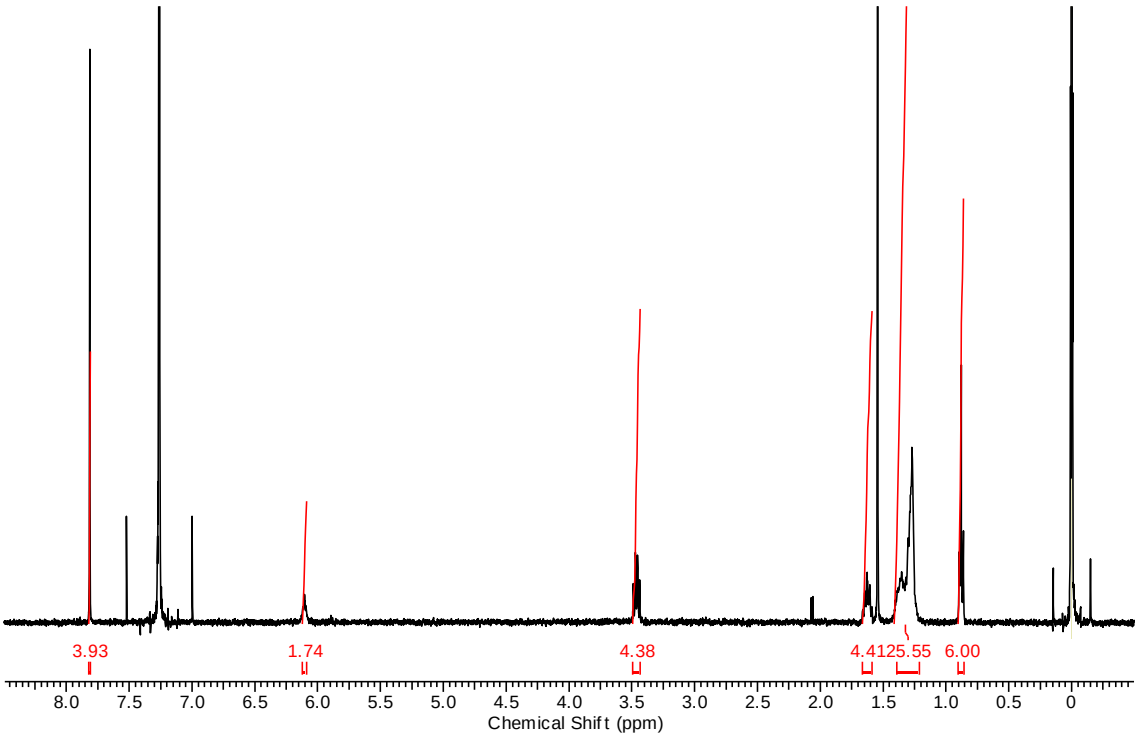

^{1}H NMR spectrum of **C9TPA** in $CDCl_3$.

N,*N*'-Didecyl-1,4-terephthalamide (**C10TPA**) Yield = 83%. Elemental analysis. Calc. for $C_{28}H_{48}N_2O_2$: C, 75.63; H, 10.88; N, 6.30. Found: C, 75.59; H, 10.89; N, 6.30. ^{1}H NMR ($CDCl_3$, 400 MHz, δ in ppm) 0.88 (6H, t, *J*=5.0 Hz, -CH_3), 1.28–1.40 (20H, m, -CH_2-), 1.63 (4H, quin, *J*=6.5 Hz, -NH-CH_2-CH_2-), 3.47 (4H, q, *J*=5.9 Hz, -NH-CH_2-), 6.12 (2H, t, *J*=4.8 Hz, -NH-), 7.81 (4H, s, Benzene). HRMS (FAB) calc. for $C_{18}H_{29}O_2H_2$: 368.2858 [$(M^+H)^+$]. Found: 368.2855.

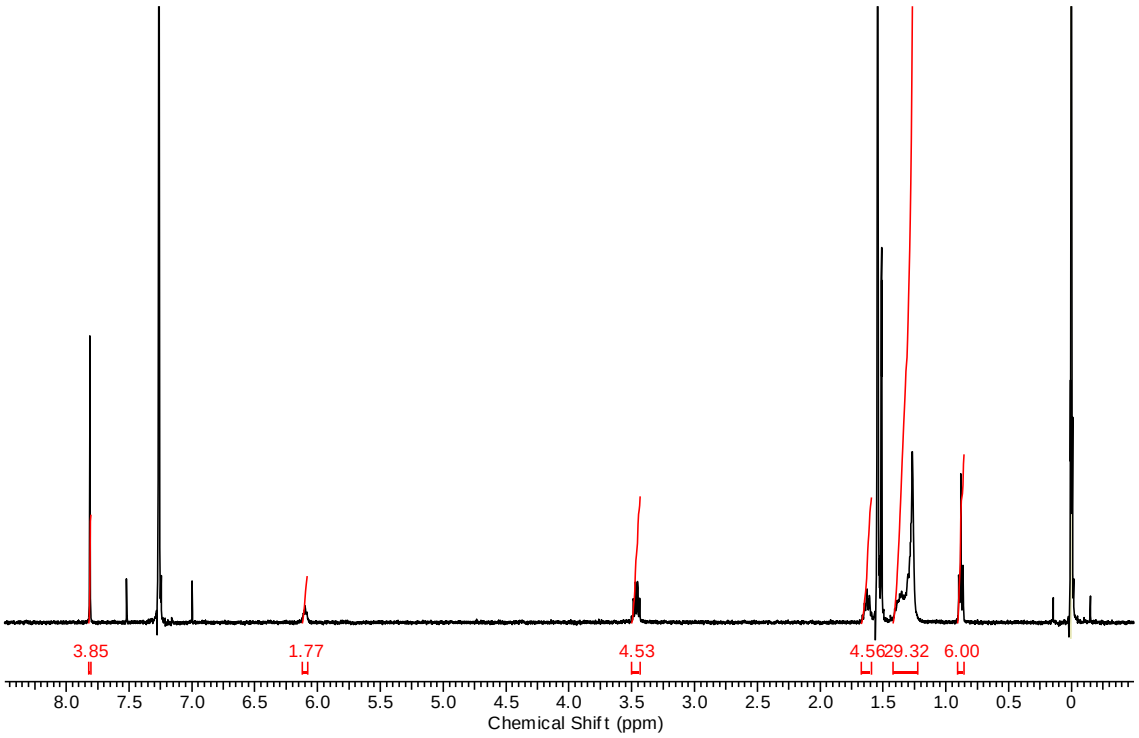

^{1}H NMR spectrum of **C10TPA** in $CDCl_3$.

N,*N*'-Dimonodecyl-1,4-terephthalamide (**C11TPA**) Yield = 78%. Elemental analysis. Calc. for $C_{28}H_{48}N_2O_2$: C, 76.22; H, 11.09; N, 5.93. Found: C, 76.03; H, 11.09; N, 6.01. ^{1}H NMR ($CDCl_3$, 400 MHz, δ in ppm) 0.88 (6H, t, *J*=6.8 Hz, -CH_3), 1.26~1.40 (32H, m, -CH_2-), 1.63 (4H, quin, *J*=7.3 Hz, -NH-CH_2-CH_2-), 3.46 (4H, q, *J*=6.7 Hz, -NH-CH_2-), 6.10 (2H, t, *J*=4.7 Hz, -NH-), 7.81 (4H, s, Benzene). HRMS (FAB) calc. for $C_{30}H_{53}O_2H_2$: 473.4107 [$(M^+H)^+$]. Found: 473.4110.

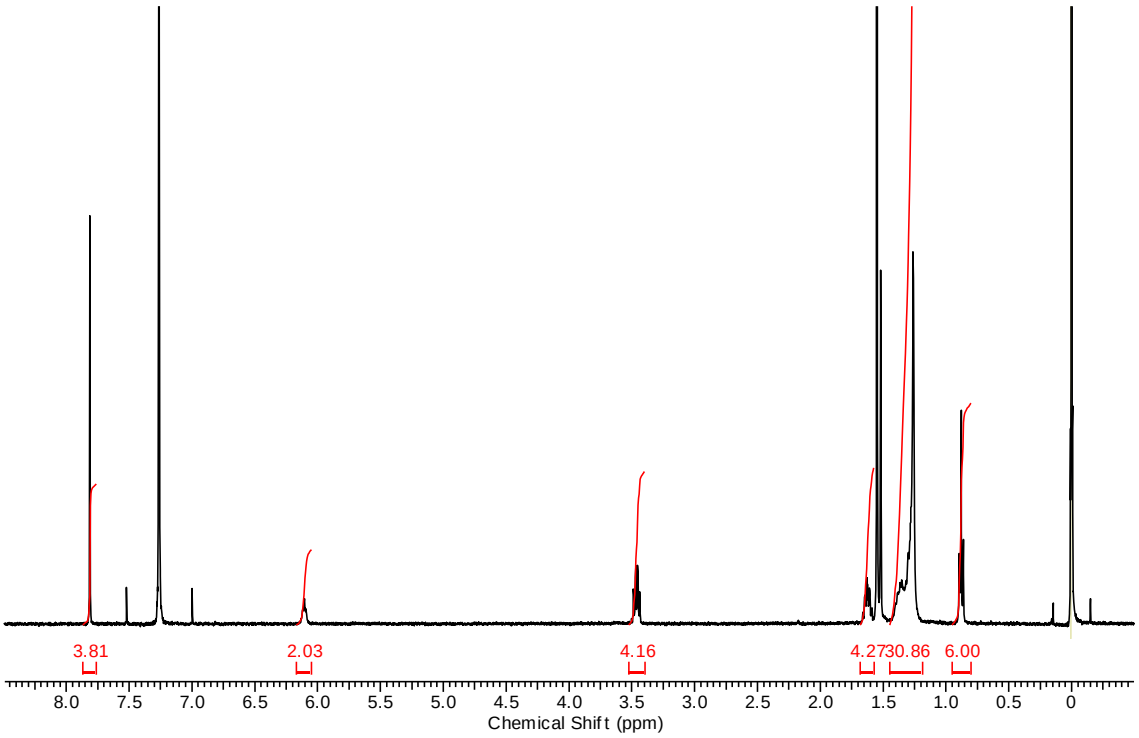

^{1}H NMR spectrum of **C11TPA** in $CDCl_3$.

N,*N*'-Didodecyl-1,4-terephthalamide (**C12TPA**) Yield = 86%. Elemental analysis. Calc. for $C_{32}H_{56}N_2O_2$: C, 76.75; H, 11.27; N, 5.59. Found: C, 76.77; H, 11.40; N, 5.63. ^{1}H NMR ($CDCl_3$, 400 MHz, δ in ppm) 0.88 (6H, t, *J*=6.5 Hz, -CH_3), 1.26~1.40 (36H, m, -CH_2-), 1.63 (4H, quin, *J*=7.1 Hz, -NH-CH_2-CH_2-), 3.46 (4H, q, *J*=6.4 Hz, -NH-CH_2-), 6.10 (2H, t, *J*=5.6 Hz, -NH-), 7.81 (4H, s, Benzene).

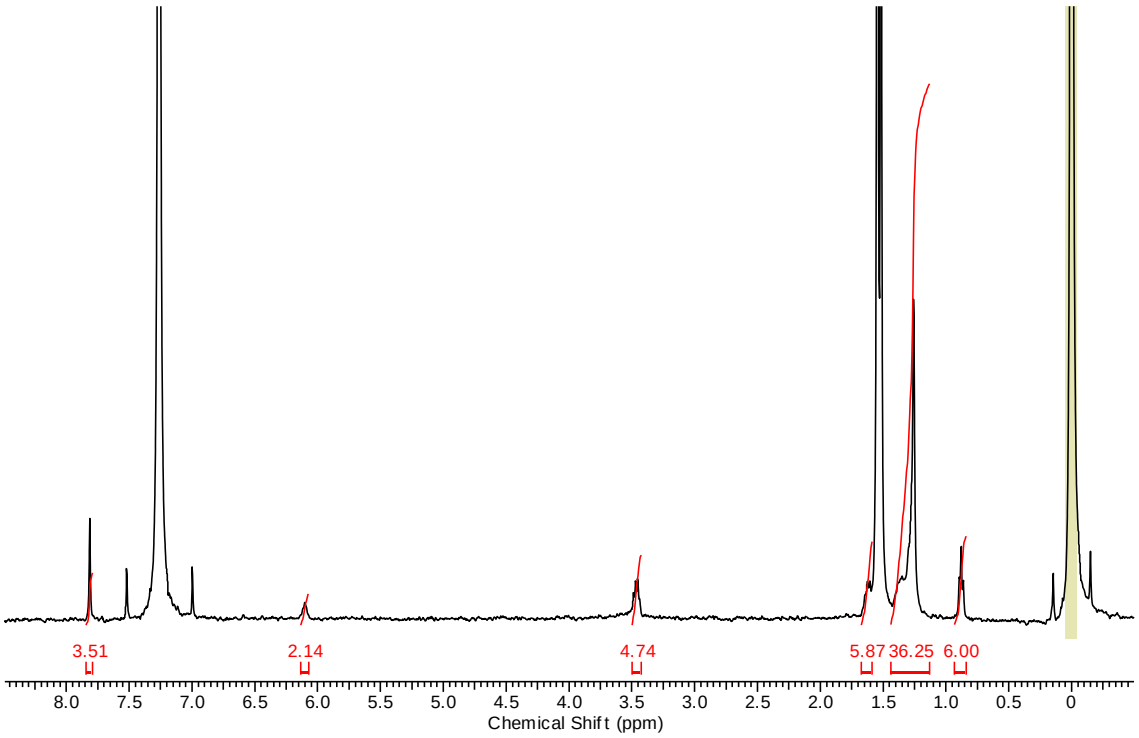

^{1}H NMR spectrum of **C12TPA** in $CDCl_3$.

N,*N*'-Ditridecyl-1,4-terephthalamide (**C13TPA**) Yield = 71%. Elemental analysis. Calc. for $C_{34}H_{60}N_2O_2$: C, 77.22; H, 11.44; N, 5.30. Found: C, 76.99; H, 11.48; N, 5.40. ^{1}H NMR ($CDCl_3$, 400 MHz, δ in ppm) 0.88 (6H, t, *J*=6.8 Hz, -CH_3), 1.26~1.38 (40H, m, -CH_2-), 1.63 (4H, quin, *J*=6.3 Hz, -NH-CH_2-CH_2-), 3.46 (4H, q, *J*=6.9 Hz, -NH-CH_2-), 7.81 (4H, s, Benzene). HRMS (FAB) calc. for $C_{34}H_{61}O_2H_2$: 529.4733 [$(M^+H)^+$]. Found: 529.4738.

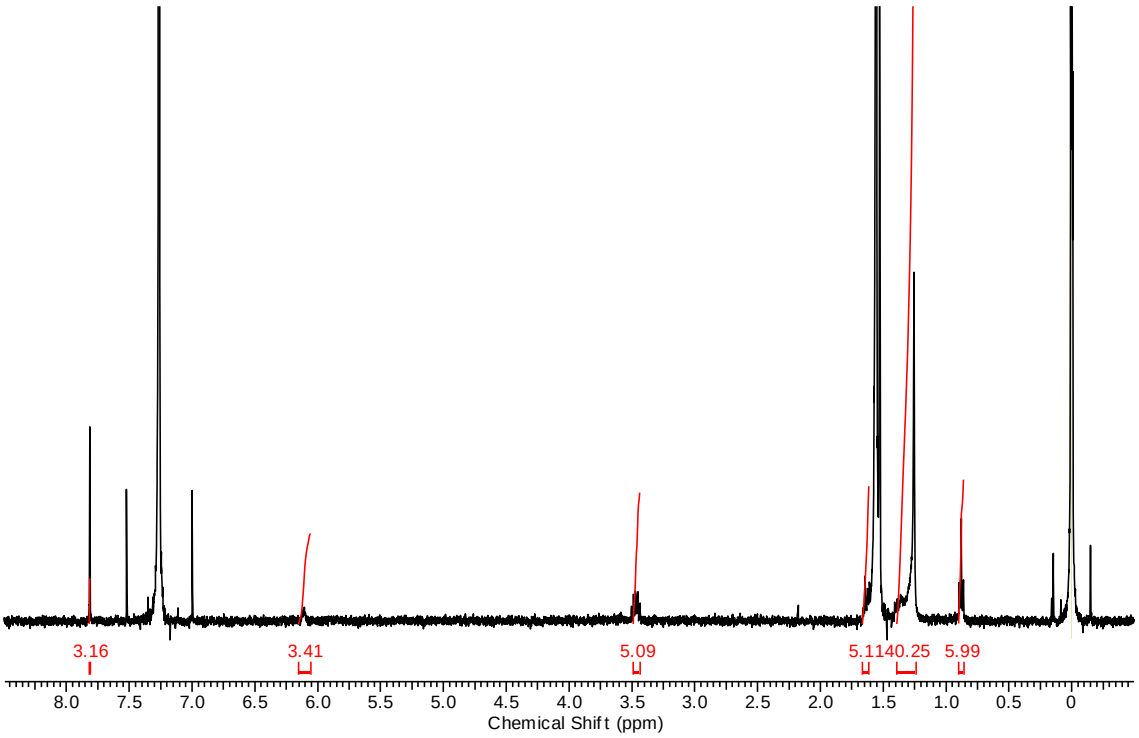

^{1}H NMR spectrum of **C13TPA** in $CDCl_3$.

N,*N*'-Ditetradecyl-1,4-terephthalamide (**C14TPA**) Yield = 75%. Elemental analysis. Calc. for $C_{36}H_{64}N_2O_2$: C, 77.64; H, 11.58; N, 5.03. Found: C, 77.62; H, 11.66; N, 5.03. ^{1}H NMR at 318 K ($CDCl_3$, 400 MHz, δ in ppm) 0.88 (6H, t, *J*=6.9 Hz, -CH_3), 1.26–1.40 (44H, m, -CH_2-), 1.62 (4H, quin, *J*=7.3 Hz, -NH-CH_2-CH_2-), 3.46 (4H, q, *J*=6.7 Hz, -NH-CH_2-), 6.04 (2H, t, *J*=5.0 Hz, -NH-), 7.80 (4H, s, Benzene).

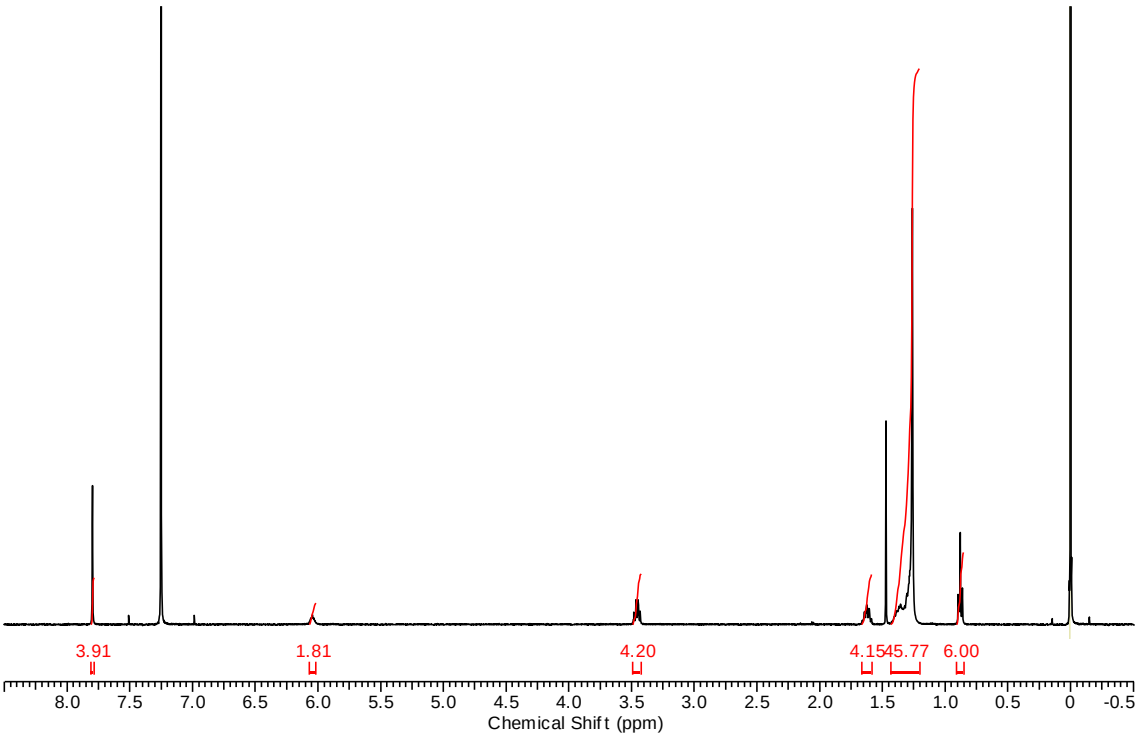

^{1}H NMR spectrum of **C14TPA** in $CDCl_3$.

N,*N*'-Dipentadecyl-1,4-terephthalamide (**C15TPA**) Yield = 89%. Elemental analysis. Calc. for $C_{38}H_{68}N_2O_2$: C, 78.02; H, 11.86; N, 4.77. Found: C, 78.02; H, 11.72; N, 4.79. ^{1}H NMR at 319 K ($CDCl_3$, 400 MHz, δ in ppm) 0.88 (6H, t, *J*=6.8 Hz, -CH_3), 1.26–1.40 (48H, m, -CH_2-), 1.63 (4H, quin, *J*=7.2 Hz, -NH-CH_2-CH_2-), 3.46 (4H, q, *J*=6.8 Hz, -NH-CH_2-), 6.04 (2H, t, J =6.1 Hz, -NH-), 7.80 (4H, s, Benzene). HRMS (FAB) calc. for $C_{38}H_{68}O_2N_2$: 585.5359 [$(M^+H)^+$]. Found : 585.5356.

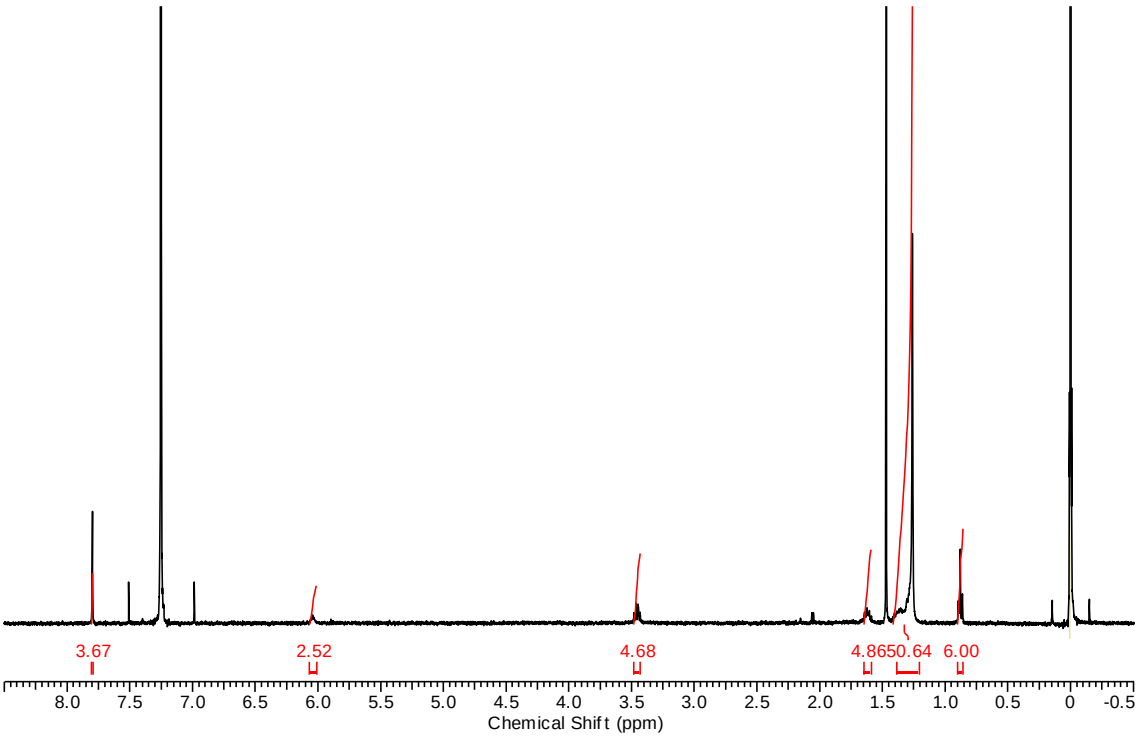

^{1}H NMR spectrum of **C15TPA** in $CDCl_3$.

N,*N*'-Dihexadecyl-1,4-terephthalamide (**C16TPA**) Yield = 84%. Elemental analysis. Calc. for $C_{40}H_{72}N_2O_2$: C, 78.37; H, 11.84; N, 4.57. Found: C, 78.35; H, 11.93; N, 4.60. ^{1}H NMR at 318 K ($CDCl_3$, 400 MHz, δ in ppm) 0.88 (6H, t, *J*=6.9 Hz, -CH_3), 1.26–1.39 (52H, m, -CH_2-), 1.62 (4H, quin, *J*=7.3 Hz, -NH-CH_2-CH_2-), 3.46 (4H, q, *J*=6.7 Hz, -NH-CH_2-), 6.04 (2H, t, *J*=5.9 Hz, -NH-), 7.80 (4H, s, Benzene).

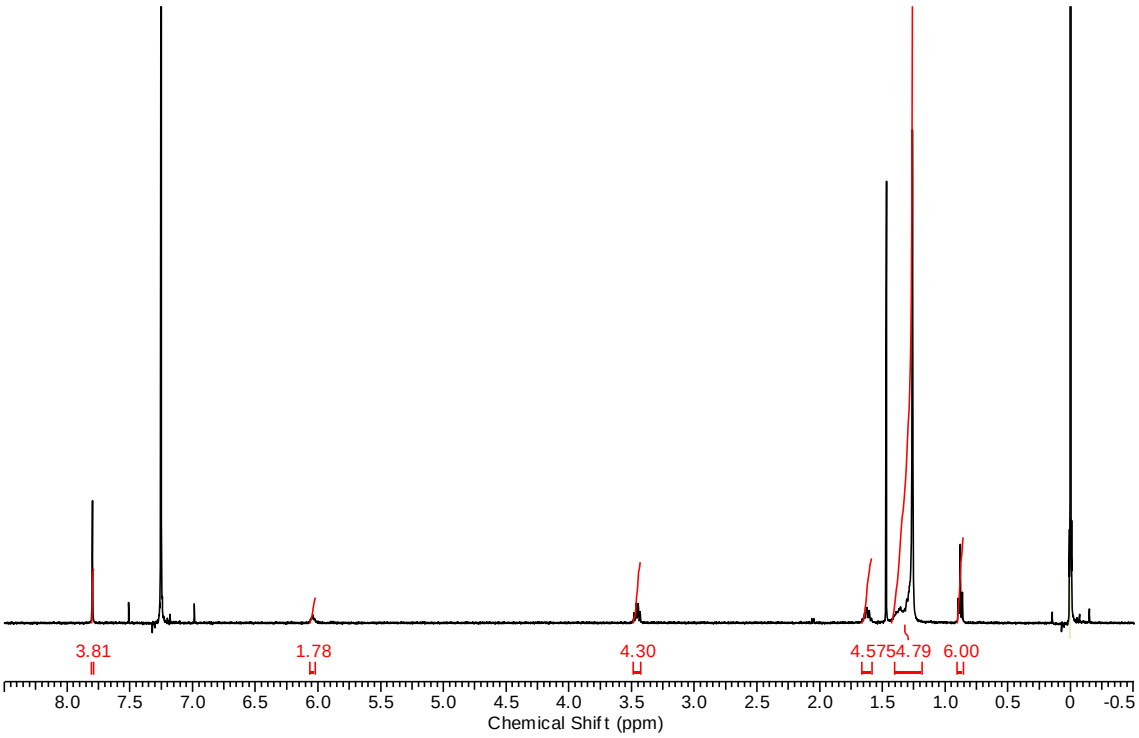

^{1}H NMR spectrum of **C16TPA** in $CDCl_3$.

N,*N*'-Dioctadecyl-1,4-terephthalamide (**C18TPA**) Yield = 90%. Elemental analysis. Calc. for $C_{44}H_{80}N_2O_2$: C, 78.98; H, 12.05; N, 4.19. Found: C, 78.98; H, 11.85; N, 4.48. ^{1}H NMR at 318 K ($CDCl_3$, 400 MHz, δ in ppm), 0.88 (6H, t, *J*=6.8 Hz, -CH_3), 1.26–1.38 (56H, m, -CH_2-), 1.62 (4H, quin, *J*=7.5 Hz, -NH-CH_2-CH_2-), 3.46 (4H, q, *J*=6.8 Hz, -NH-CH_2-), 6.04 (2H, t, *J*=5.0 Hz, -NH-), 7.80 (4H, s, Benzene).

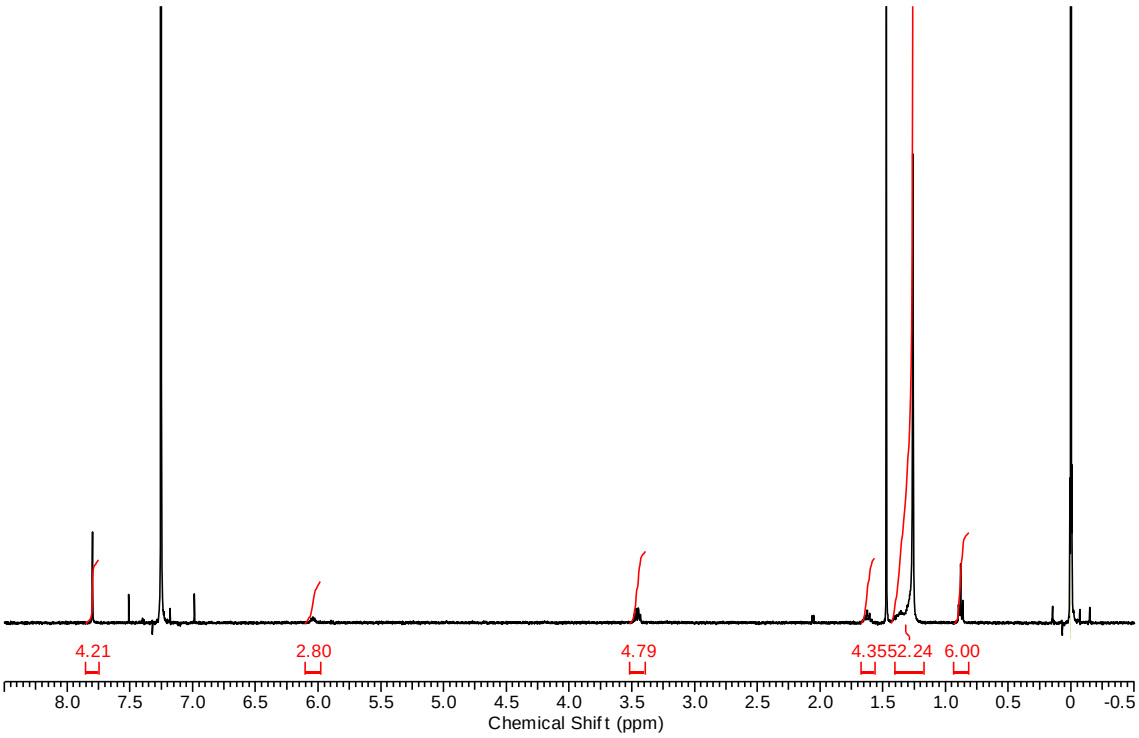

^{1}H NMR spectrum of **C18TPA** in $CDCl_3$.

Physical measurements. ^{1}H NMR spectra were recorded using a Bruker Avance III 400 NMR spectrometer, and chemical shifts (δ, ppm) were obtained relative to tetramethylsilane as an internal standard. Temperature-dependent infrared (IR, 400–4000 cm^{-1}) spectra were measured using a Thermo Fisher Scientific Nicolet 6700 spectrophotometer with a resolution of 1 cm^{-1} using KBr pellets. The surface morphologies of the molecular assemblies on a highly oriented pyrolytic graphite (HOPG) substrate were examined by scanning electron microscopy (SEM, JEOL JSM-5400F) and atomic force microscopy (AFM, Hitachi 5100N). Thin films were fabricated on the surfaces of HOPG and mica substrates using the cast method in a chloroform solution. Thermogravimetric–differential thermal analysis (TG–DTA) was conducted using a Rigaku Thermo plus TG8120 thermal analysis station with Al_2O_3 as a reference in the temperature range of 300–780 K at a heating rate of 5 K min^{-1} under a N_2 atmosphere. Differential scanning calorimetry (DSC) was performed using a METTLER thermal analysis DSC1-TS station using Al_2O_3 as a reference in the temperature range of 173–550 K at heating and cooling rates of 5 K min^{-1} under a N_2 atmosphere. Temperature-dependent powder X-ray diffraction (PXRD) patterns were measured using a Rigaku RINT-Ultima III diffractometer with Cu Kα radiation at an irradiation wavelength

of λ = 1.54187 Å. Temperature-dependent dielectric constants were measured using the two-probe alternating current impedance method (HP4194A) over a frequency range of 10^2 to 10^6 Hz. Ferroelectric polarization–electric field hysteresis (*P*–*E*) curves were acquired using a commercially available ferroelectric tester (Precision LC, Radiant Technologies). Solid state samples of **CnTPA** were fabricated on an indium tin oxide (ITO) glass (SZ−A311P6N), which was sandwiched between the corresponding ITO glass to form a dielectric measurement cell with an average electrode gap of 2 μm.

Crystal structure determination. Single crystals were obtained by slowly cooling the crystallization solution. Crystallographic data were acquired using a Rigaku RAPID II diffractometer equipped with a rotating anode fitted with a multilayer confocal optic and using Cu Kα (λ = 1.54187 Å) radiation from a graphite monochromator. Structural refinement was performed using the full-matrix least-squares method on F_2. Calculations were conducted using crystal structure software packages.[91, 92] All parameters except for those of H atoms were refined using anisotropic temperature factors. Crystallographic data of **C5TPA** ($C_{18}H_{28}N_2O_2$): F.W. = 304.43; crystal dimensions: 0.30 × 0.20 × 0.10 mm^3; T = 250 K; Triclinic P–1 (#2); a = 5.0874(6); b = 5.1180(6); c = 16.8328(18) Å; α = 90.632(6), β = 97.129(7), γ = 93.262(7)°; V = 434.12(8) $Å^3$; Z = 1; d_{calcd} = 1.164 g cm^{-3}; μ = 5.976 cm^{-1}; collected: 5123; unique: 1549; R_{int} = 0.0373; R_1= 0.0474; R_{all} = 0.0494; R_w = 0.1366; G.O.F = 1.073; and the maximum and minimum peaks on the final difference Fourier map corresponded to +0.19 and −0.32 e^- $Å^{-3}$. CCDC-2110544.

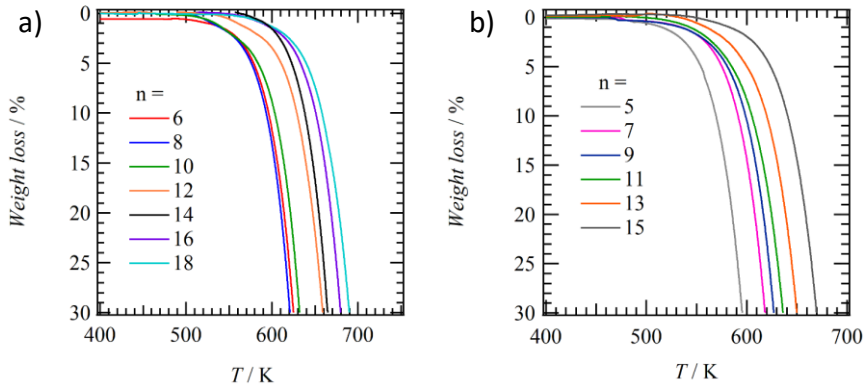

Figure S1. TG charts of **CnTPA**. a) Even-number and b) odd-number derivatives.

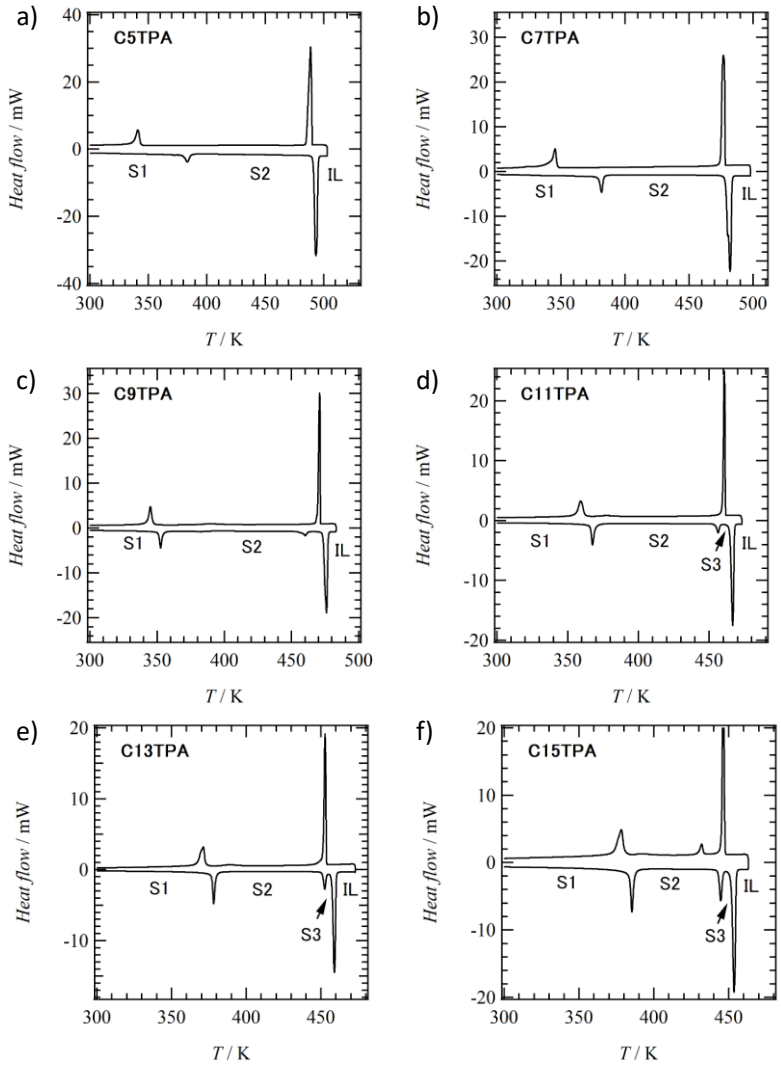

Figure S2. DSC charts of the odd-number **CnTPAs**. a) **C5TPA**, b) **C7TPA**, c) **C9TPA**, d) **C11TPA,** e) **C13TPA**, and f) **C15TPA**.

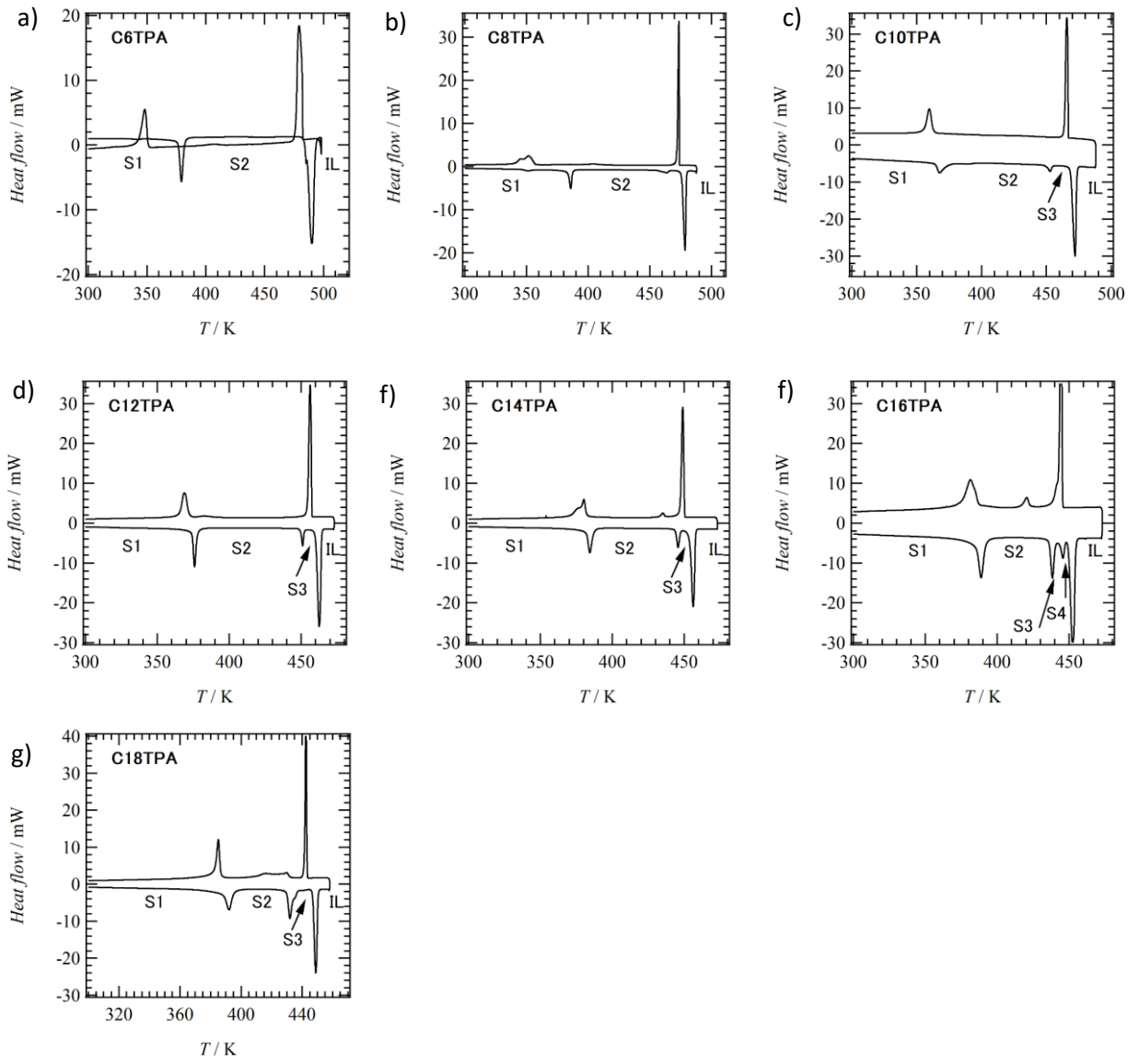

Figure S3. DSC charts of the even-number **CnTPAs**. a) **C6TPA**, b) **C8TPA**, c) **C10TPA**, d) **C12TPA,** e) **C14TPA**, f) **C16TPA**, and g) **C18TPA**.

Table S1. Phase transition behaviors of **CTPA**.

Comp.	Transition[a]	$T_{S\text{-}S}$, K	ΔH, kJ mol^{-1}	ΔS, kJ mol^{-1} K^{-1}	$\Sigma\Delta H$,[b] kJ mol^{-1}	$\Sigma\Delta S$,[b] kJ mol^{-1} K^{-1}
C5TPA	S1−S2	378.6	−5.38	−14.2	−48.2	−101.3
	S2−IL	490.6	−42.8	−87.1		
C6TPA	S1−S2	373.7	−8.6	−22.7	−41.4	−90.9
	S2−IL	480.8	−32.8	−68.2		
C7TPA	S1−S2	379.3	−7.3	−19.3	−55.8	−120.7
	S2−IL	478.5	−48.5	−101.4		
C8TPA	S1−S2	346.0	−1.9	−5.46	−57.2	−121.3
	S2−S3	456.2	−3.7	−8.17		
	S3−IL	471.6	−51.6	−107.5		
C9TPA	S1−S2	350.7	−9.7	−27.6	−63.2	−141.0
	S2−S3	453.6	−4.0	−8.9		
	S3−IL	473.3	−49.5	−104.5		
C10TPA	S1−S2	362.8	−12.4	−34.0	−68.6	−154.5
	S2−S3	448.5	−3.9	−8.78		
	S3−IL	465.2	−52.3	−111.7		
C11TPA	S1−S2	366.0	−12.2	−17.2	−68.2	−140.7
	S2−S3	454.4	−4.5	−12.5		
	S3−IL	464.5	−51.5	−111.0		
C12TPA	S1−S2	360.6	−19.2	−51.5	−81.6	−187.8
	S2−S3	445.6	−6.3	−14.0		
	S3−IL	455.5	−56.1	−122.3		
C13TPA	S1−S2	376.5	−17.2	−45.8	−81.0	−185.6
	S2−S3	450.9	−9.5	−21.0		
	S3−IL	460.2	−54.3	−118.8		
C14TPA	S1−S2	380.7	−20.4	−53.5	−82.4	−191.0
	S2−S3	441.9	−10.5	−23.8		
	S3−IL	449.7	−51.5	−113.7		

C15TPA	S1−S2	383.2	−20.0	−52.2	−75.0	−174.1
	S2−S3	442.8	−1.4	−3.1		
	S3−IL	451.4	−53.6	−118.8		
C16TPA	S1−S2	381.6	−21.8	−56.7	−92.8	−216.6
	S2−S3	441.7	−15.2	−35.0		
	S3−S4	433.9	−8.6	−19.5		
	S4−IL	447.9	−47.2	−105.4		
C18TPA	S1−S2	385.8	−25.5	−65.9	−98.7	−232.0
	S2−S3	427.5	−25.7	−59.7		
	(S3−S4)	427.5	–	–		
	S4−IL	445.1	−47.5	−106.4		

[a] IL is isotropic liquid. [b] ΣΔH and ΣΔS were the sum of all phase transition enthalpy and entropy, respectively.

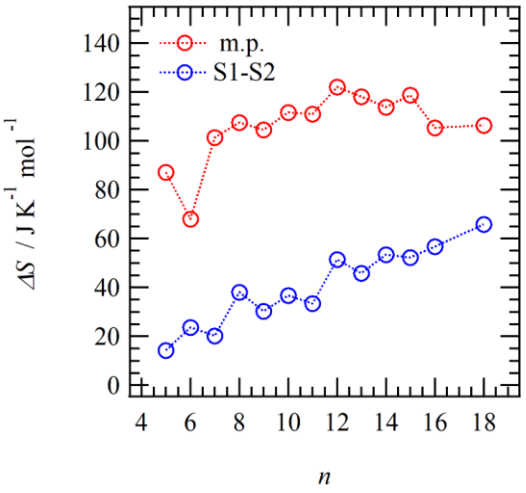

Figure S4. Even–odd effect of transition enthalpy change (ΔS) of S1–S2 phase transition (blue) and melting point (red).

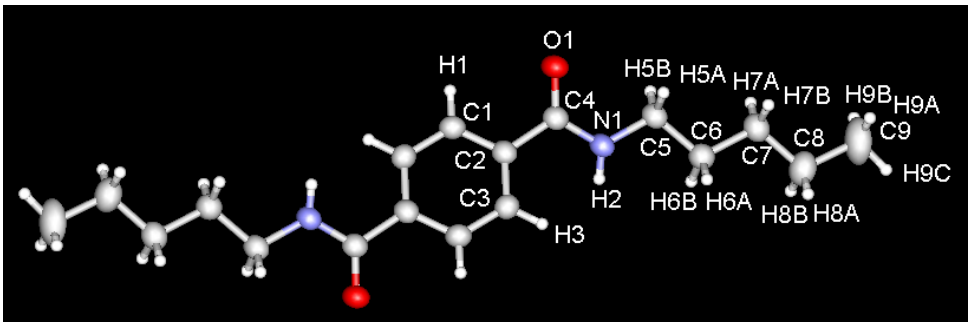

Figure S5. Atomic numbering scheme of **C5TPA** for the single-crystal X-ray structural analysis.

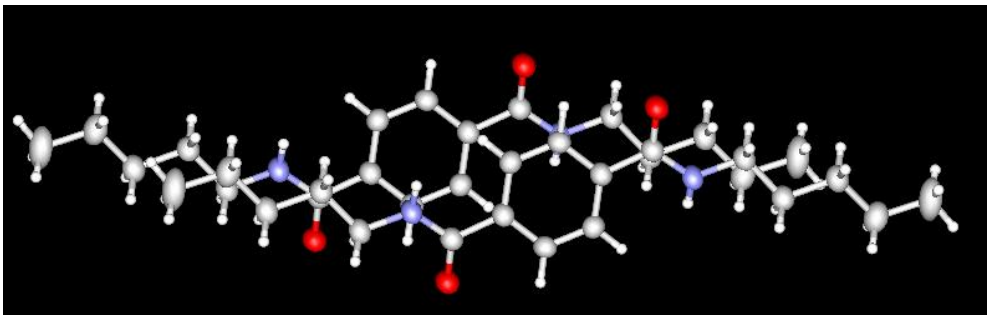

Figure S6. The π-π overlap mode of **C5TPA**.

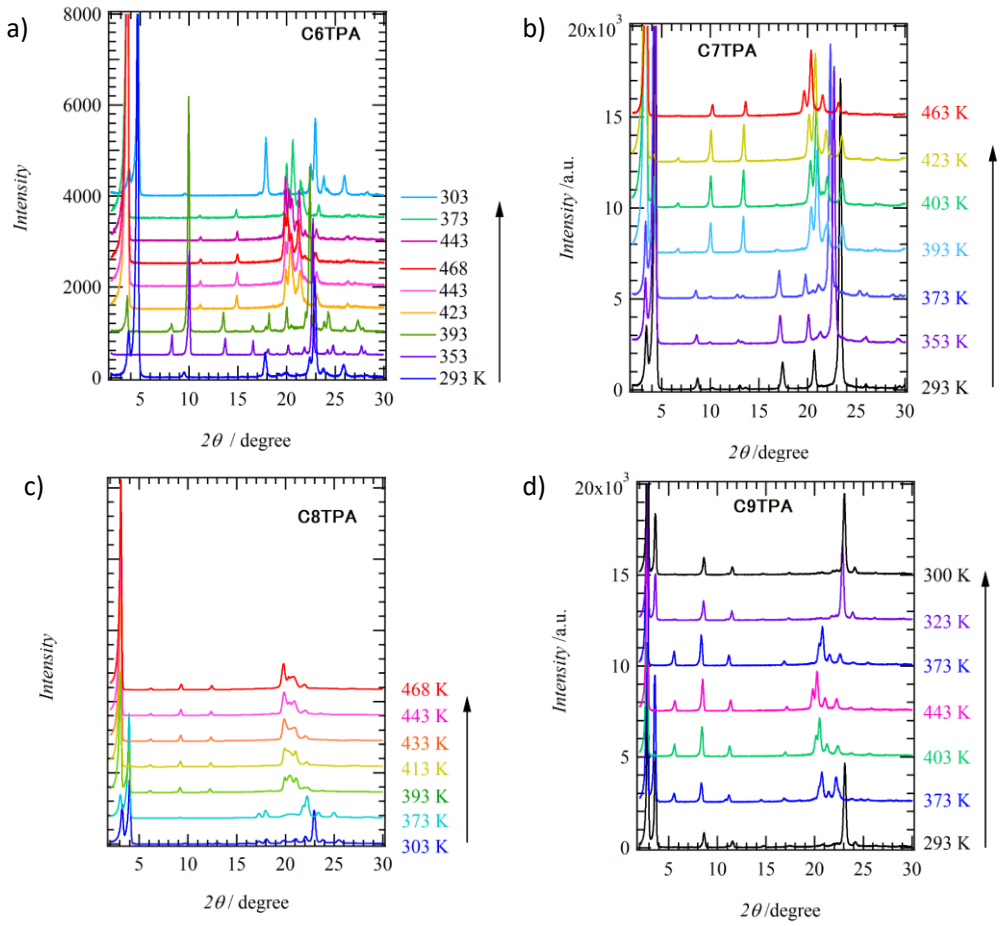

Figure S7. *T*-dependent PXRD patterns of a) **C6TPA**, b) **C7TPA**, c) **C8TPA**, and d) **C9TPA**.

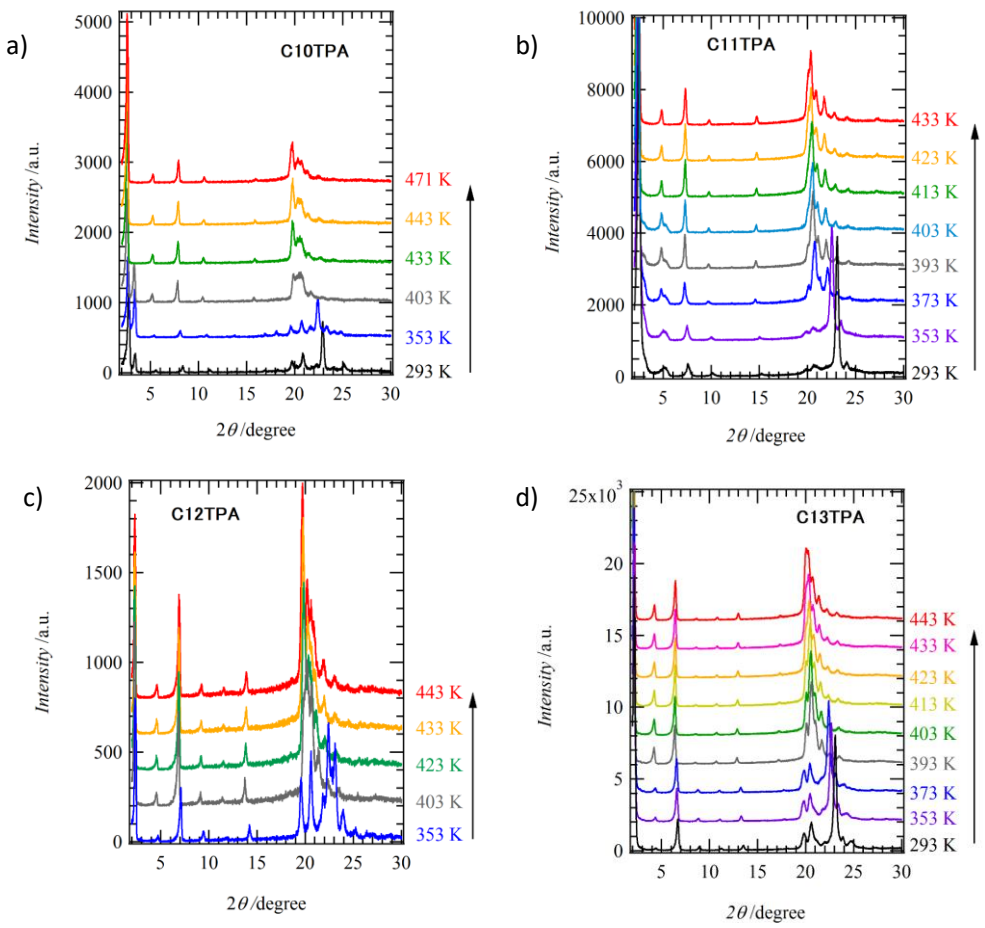

Figure S8. *T*-dependent PXRD patterns of a) **C10TPA**, b) **C11TPA**, c) **C12TPA**, and d) **C13TPA**.

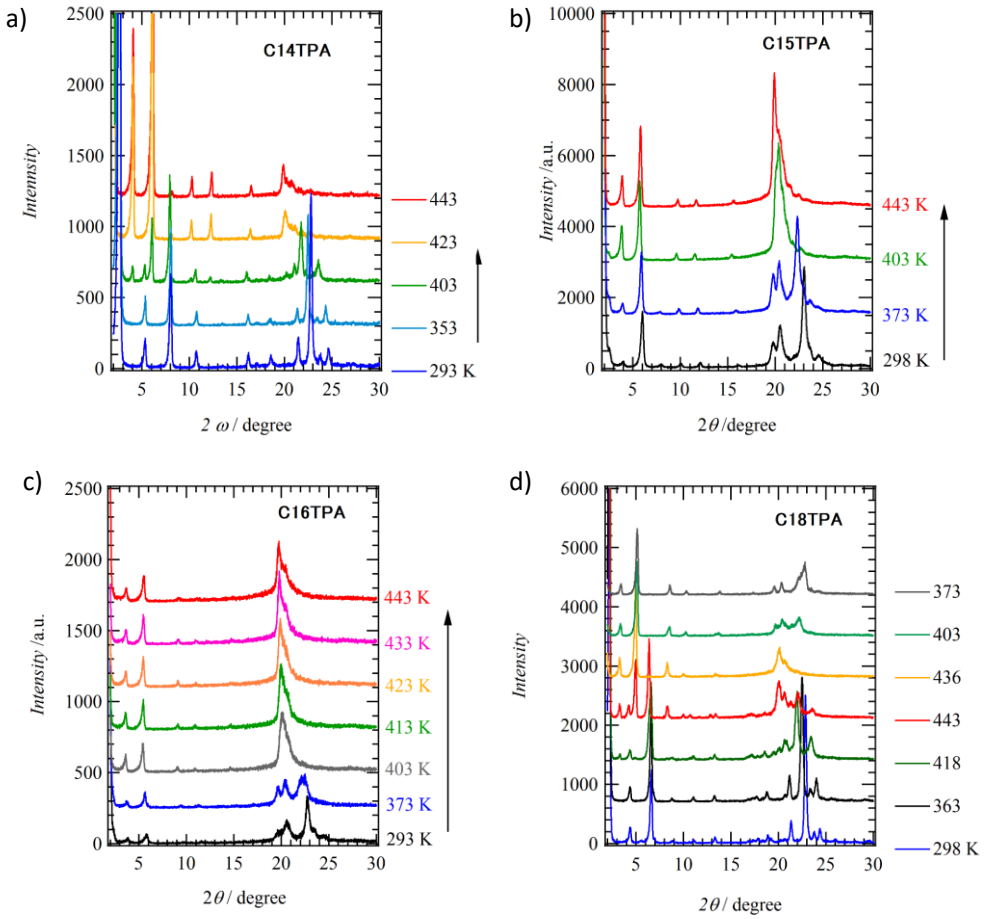

Figure S9. *T*-dependent PXRD patterns of a) **C14TPA**, b) **C15TPA**, c) **C16TPA**, and d) **C18TPA**.

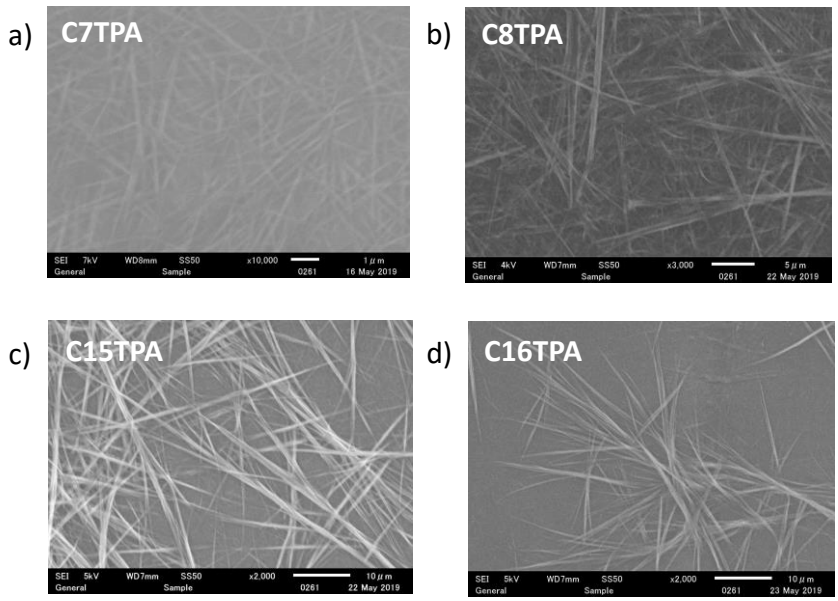

Figure S10. SEM images of a) **C7TPA** (area: 1×1 μm^2), b) **C8TPA** (area: 5×5 μm^2), c) **C15TPA** (area: 10×10 μm^2), and d) **C16TPA** (area: 10×10 μm^2).

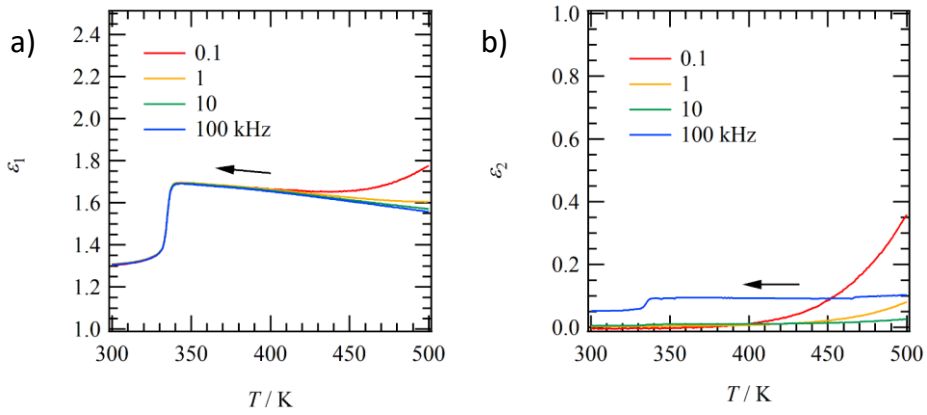

Figure S11. The *T*- and *f*-dependent a) ε_1 and b) ε_2 responses of **C5TPA** in the cooling process from IL.

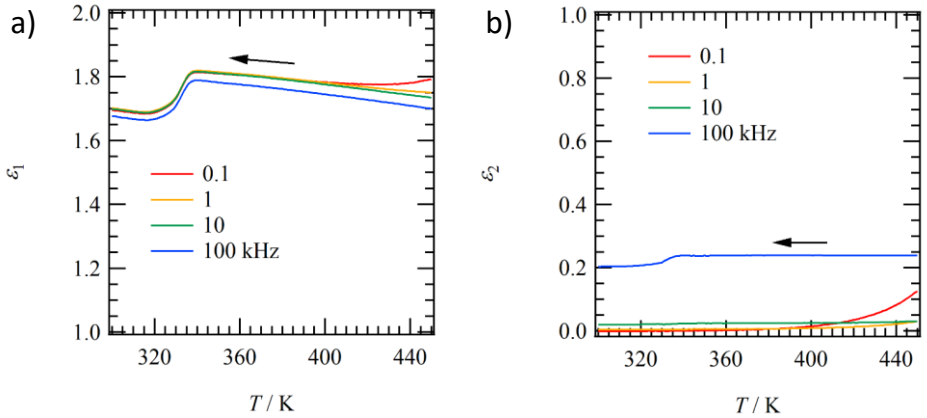

Figure S12. The *T*- and *f*-dependent a) ε_1 and b) ε_2 responses of **C6TPA** in the cooling process from IL.

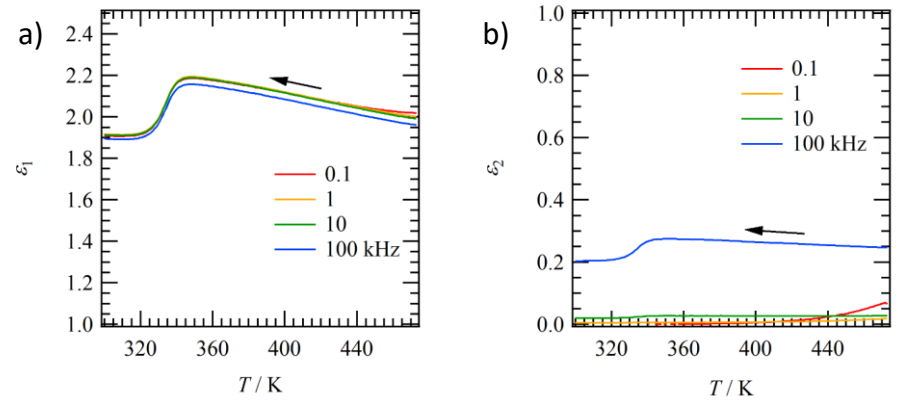

Figure S13. The *T*- and *f*-dependent a) ε_1 and b) ε_2 responses of **C7TPA** in the cooling process from IL.

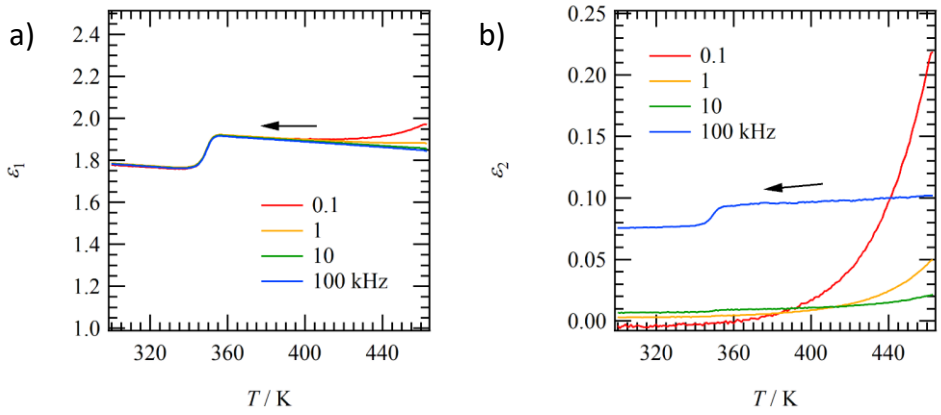

Figure S14. The *T*- and *f*-dependent a) ε_1 and b) ε_2 responses of **C8TPA** in the cooling process from IL.

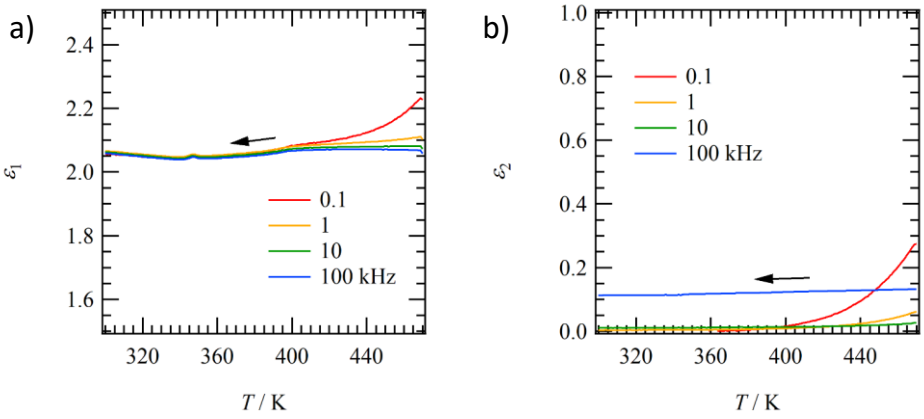

Figure S15. The *T*- and *f*-dependent a) ε_1 and b) ε_2 responses of **C9TPA** in the cooling process from IL.

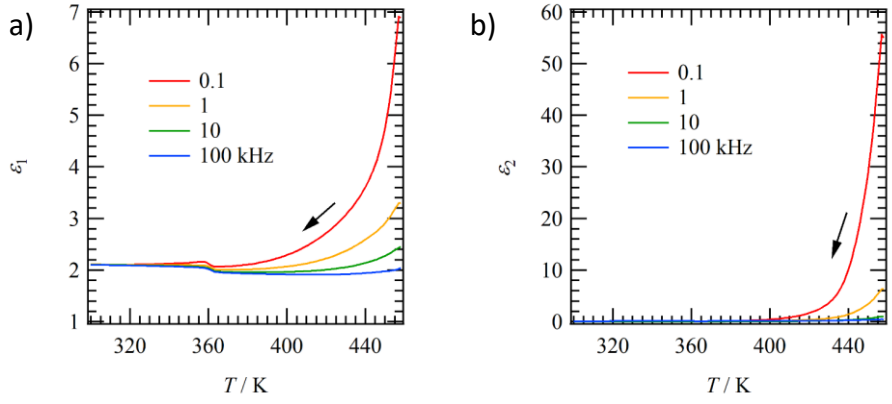

Figure S16. The *T*- and *f*-dependent a) ε_1 and b) ε_2 responses of **C10TPA** in the cooling process from IL.

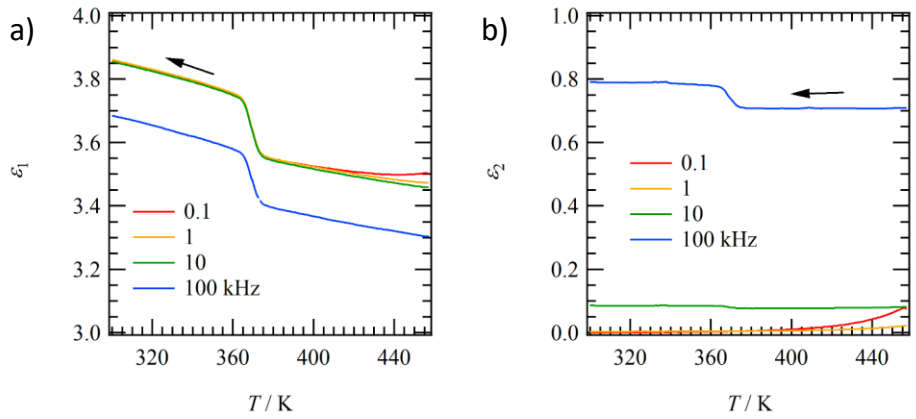

Figure S17 The *T*- and *f*-dependent a) ε_1 and b) ε_2 responses of **C11TPA** in the cooling process from IL.

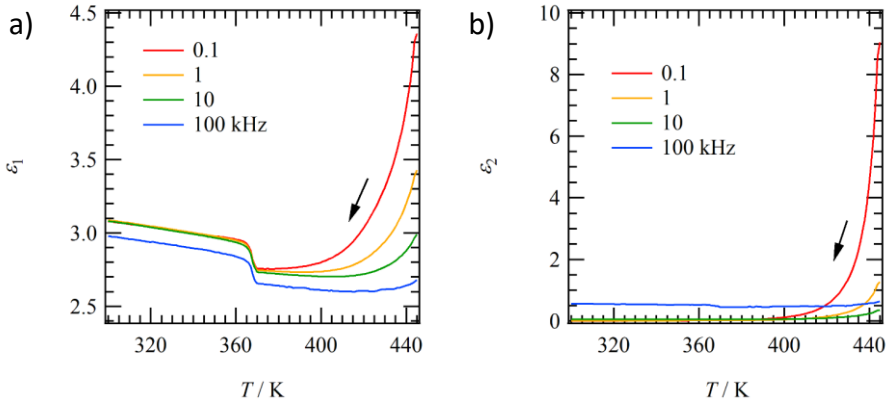

Figure S18. The *T*- and *f*-dependent a) ε_1 and b) ε_2 responses of **C12TPA** in the cooling process from IL.

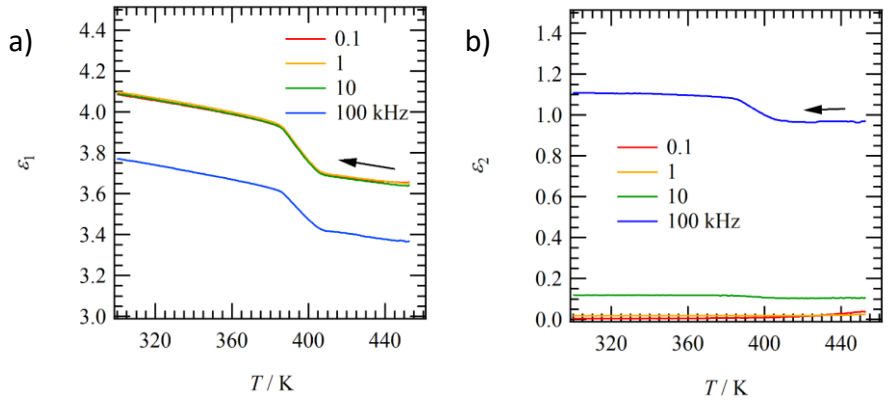

Figure S19. The *T*- and *f*-dependent a) ε_1 and b) ε_2 responses of **C13TPA** in the cooling process from IL.

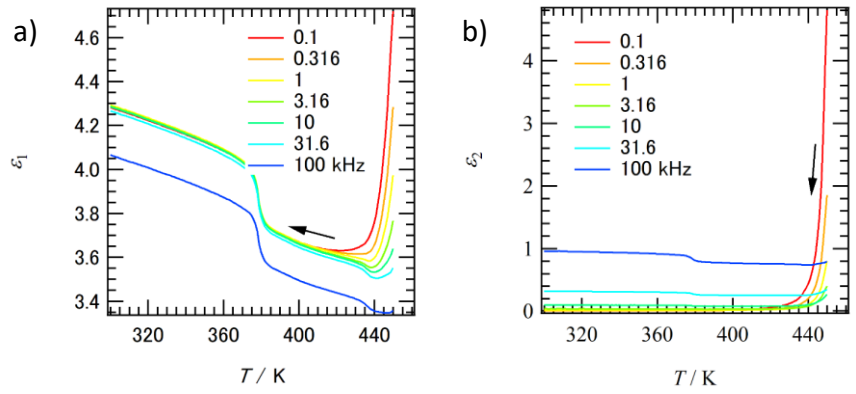

Figure S20. The *T*- and *f*-dependent a) ε_1 and b) ε_2 responses of **C14TPA** in the cooling process from IL.

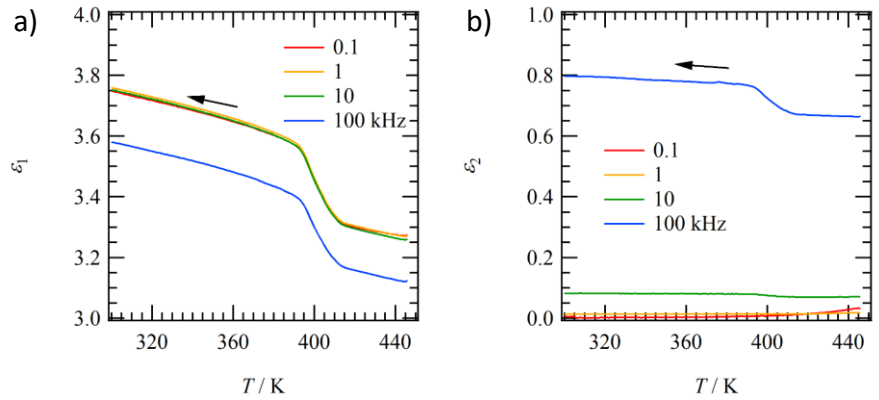

Figure S21. The *T*- and *f*-dependent a) ε_1 and b) ε_2 responses of **C15TPA** in the cooling process from IL.

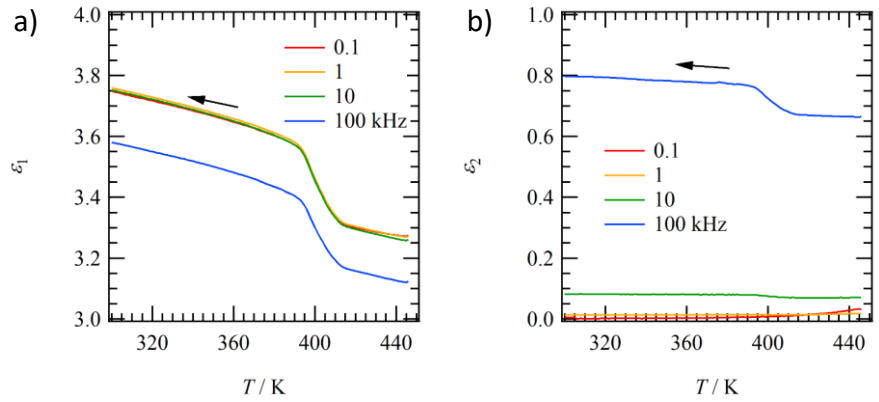

Figure S22. The *T*- and *f*-dependent a) ε_1 and b) ε_2 responses of **C16TPA** in the cooling process from IL.

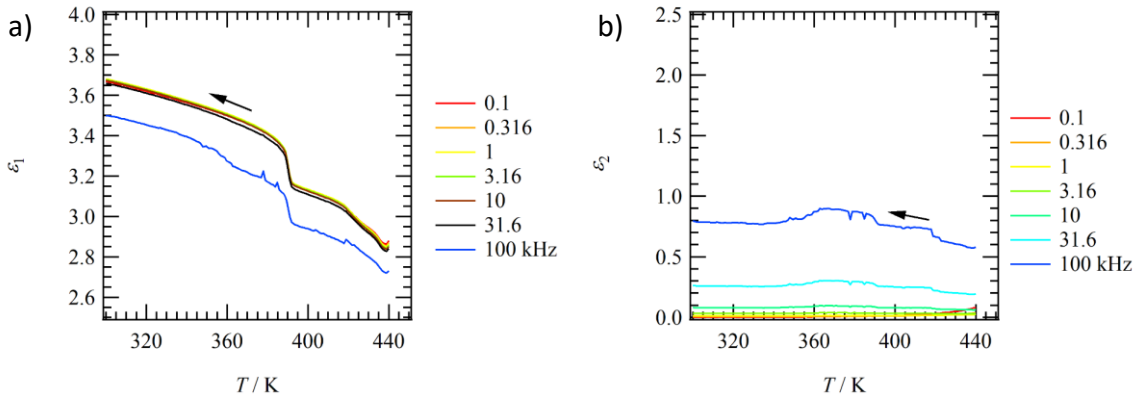

Figure S23. The *T*- and *f*-dependent a) ε_1 and b) ε_2 responses of **C18TPA** in the cooling process from IL.

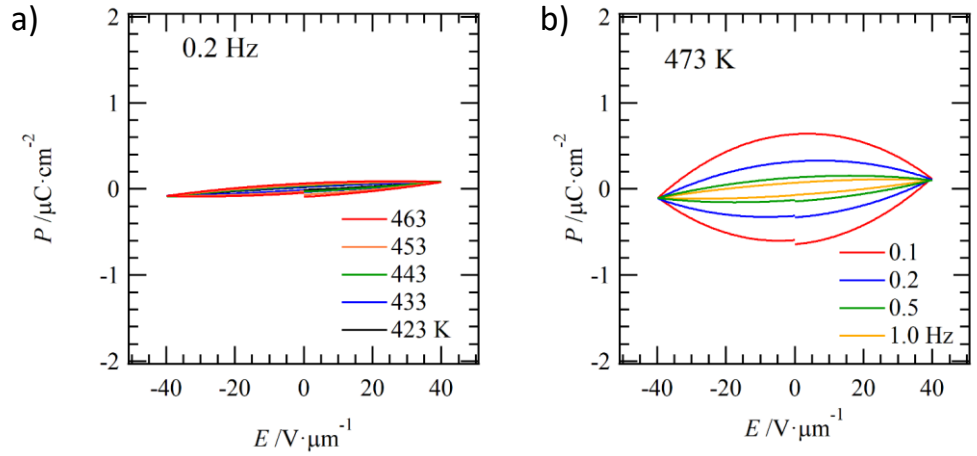

Figure S24. The *P* – *E* hysteresis measurement of **C5TPA** for a) the *T*-dependence at *f* = 0.2 Hz and b) the *f*-dependence at 473 K.

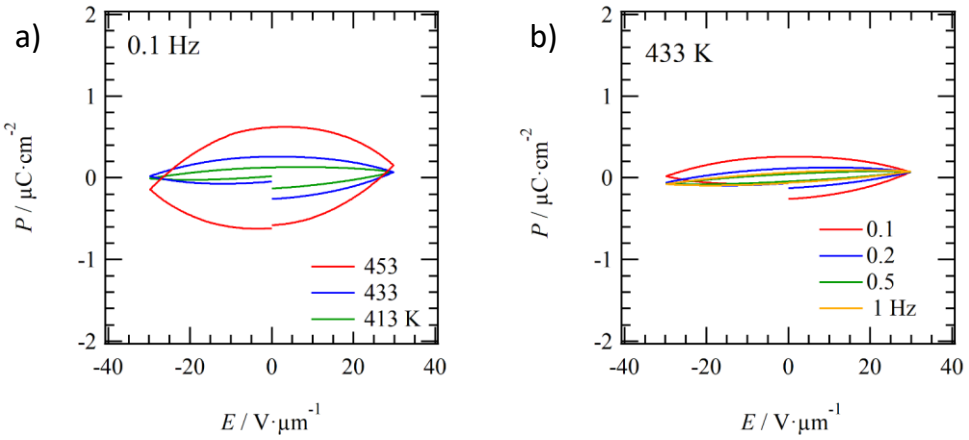

Figure S25. The *P* – *E* hysteresis measurement of **C6TPA** for a) the *T*-dependence at *f* = 0.1 Hz and b) the *f*-dependence at 433 K.

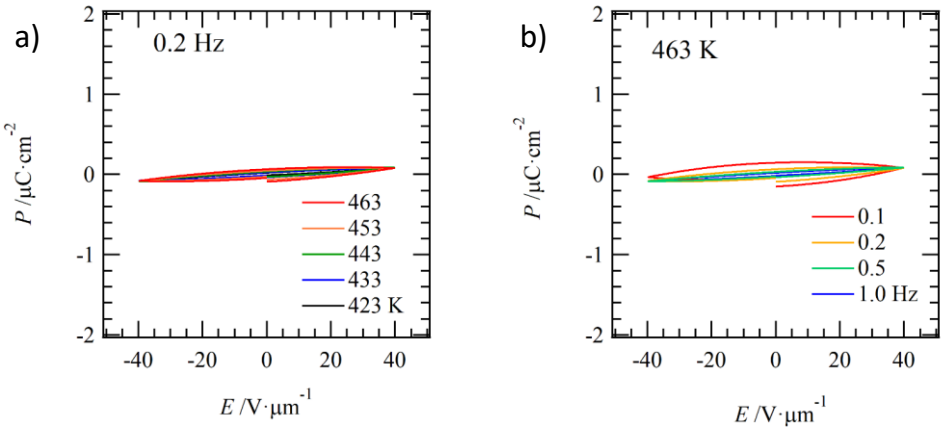

Figure S26. The *P* – *E* hysteresis measurement of **C7TPA** for a) the *T*-dependence at *f* = 0.1 Hz and b) the *f*-dependence at 453 K.

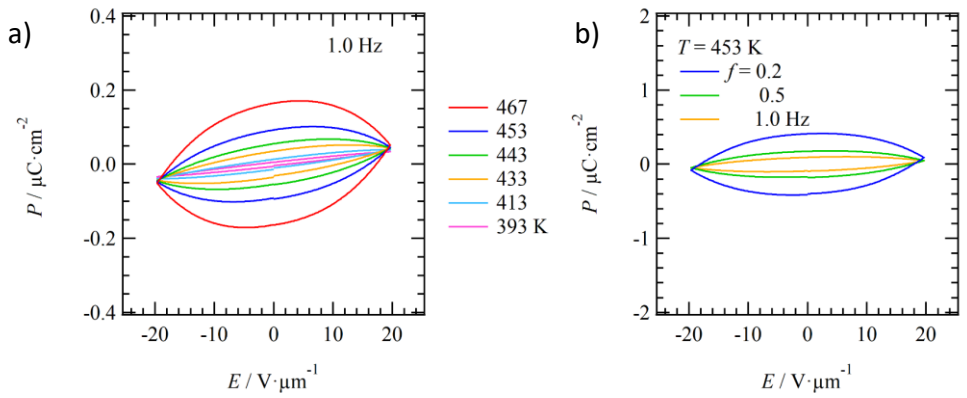

Figure S27. The *P* – *E* hysteresis measurement of **C8TPA** for a) the *T*-dependence at *f* = 0.1 Hz and b) the *f*-dependence at 453 K.

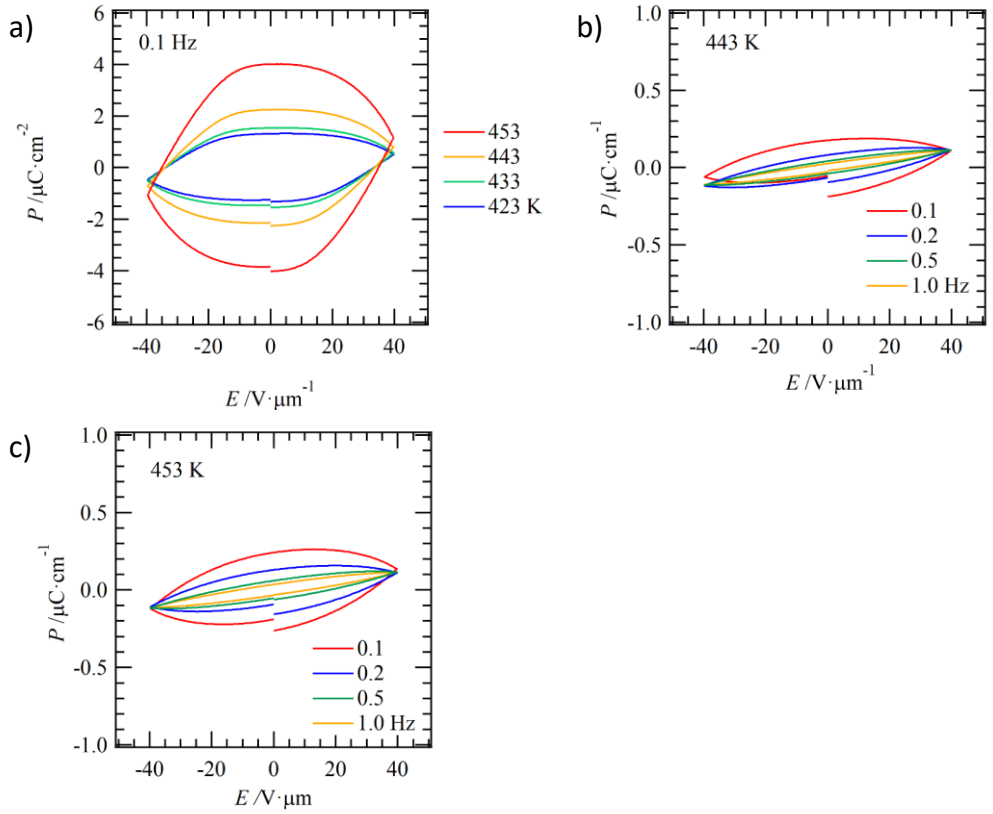

Figure S28. The *P* – *E* hysteresis measurement of **C9TPA** for a) the *T*-dependence at *f* = 0.1 Hz, b) the *f*-dependence at 443 K, and c) the *f*-dependence at 453 K.

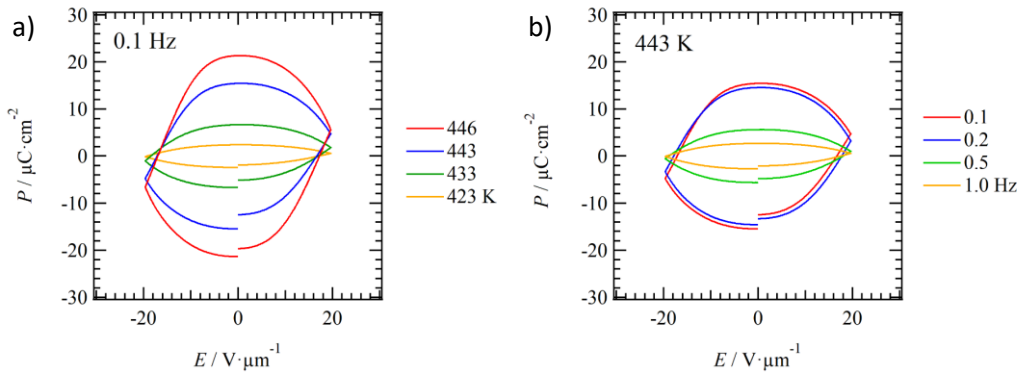

Figure S29. The *P* – *E* hysteresis measurement of **C10TPA** for a) the *T*-dependence at *f* = 0.1 Hz and b) the *f*-dependence at 443 K.

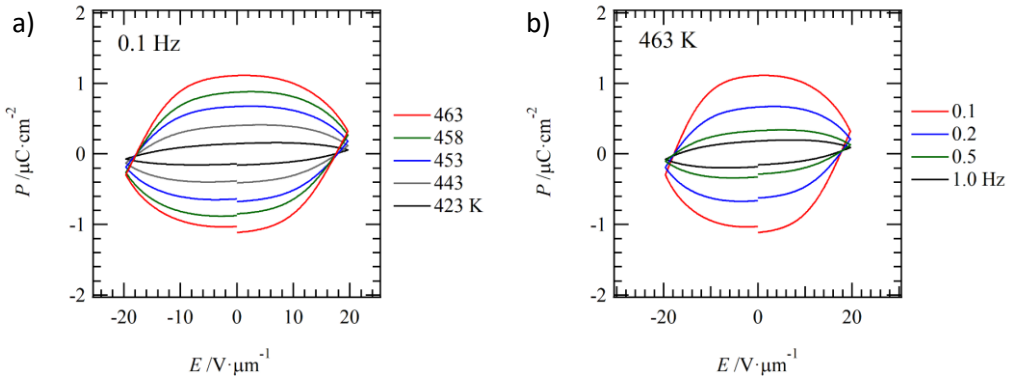

Figure S30. The *P* – *E* hysteresis measurement of **C11TPA** for a) the *T*-dependence at *f* = 0.1 Hz and b) the *f*-dependence at 463 K.

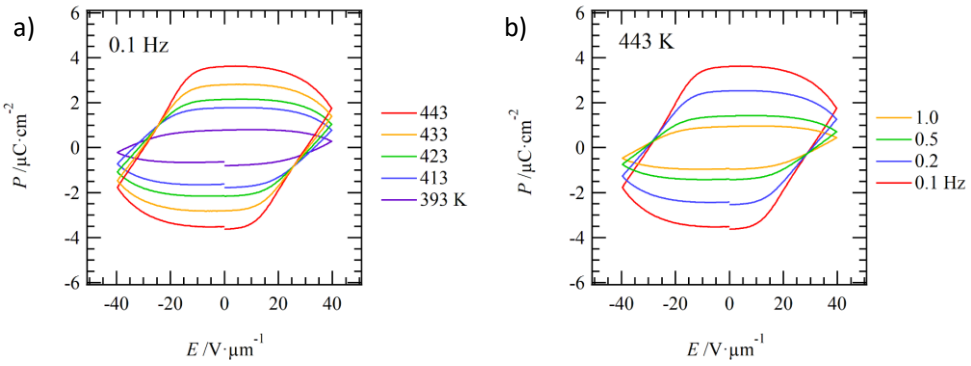

Figure S31. The *P* – *E* hysteresis measurement of **C12TPA** for a) the *T*-dependence at *f* = 0.1 Hz and b) the *f*-dependence at 443 K.

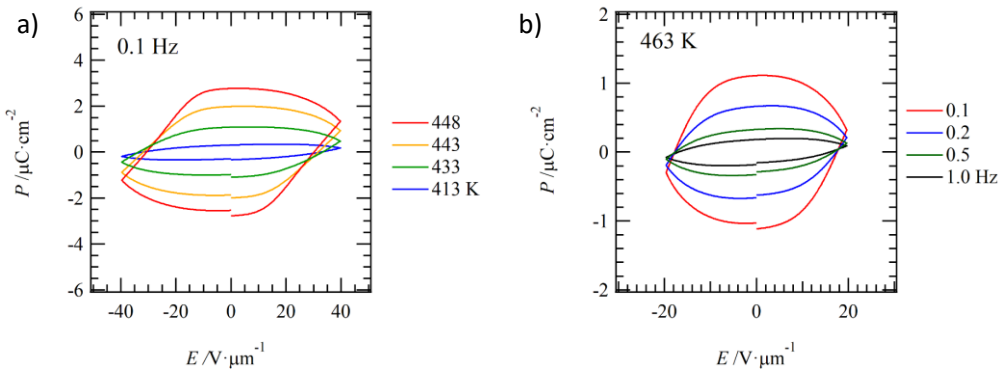

Figure S32. The *P* – *E* hysteresis measurement of **C13TPA** for a) the *T*-dependence at *f* = 0.1 Hz and b) the *f*-dependence at 463 K.

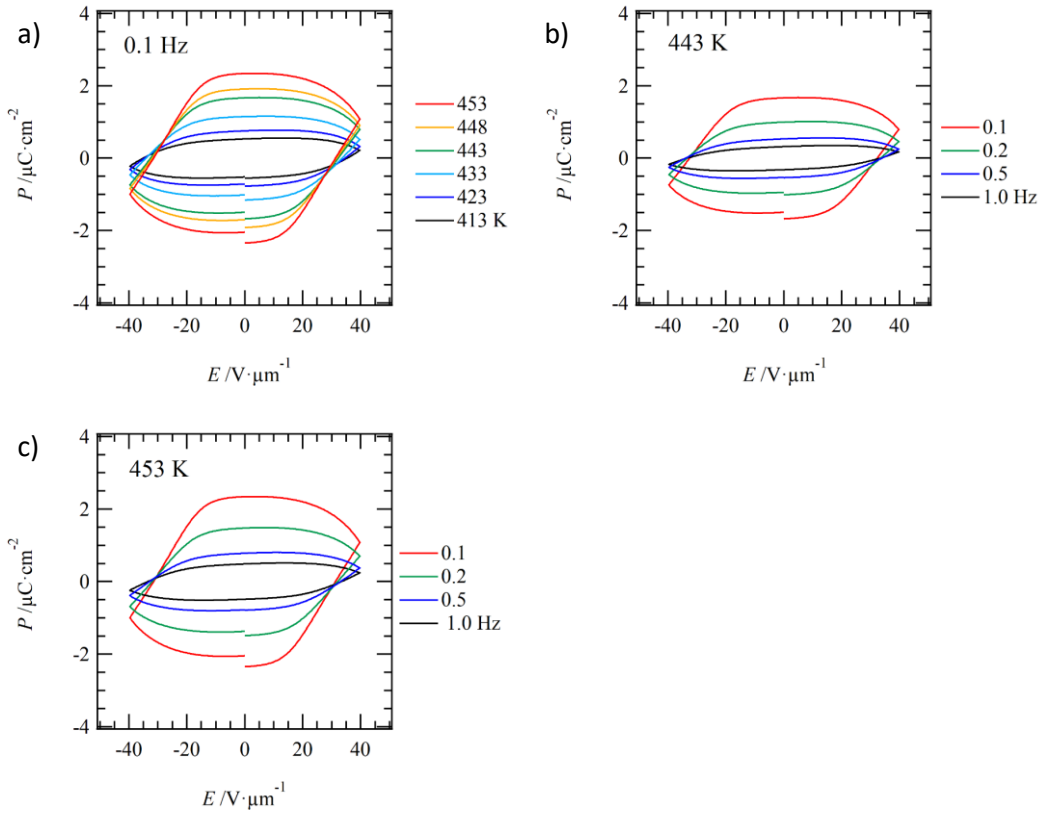

Figure S33. The *P* – *E* hysteresis measurement of **C14TPA** for a) the *T*-dependence at *f* = 0.1 Hz, b) the *f*-dependence at 443 K, and c) the *f*-dependence at 453 K.

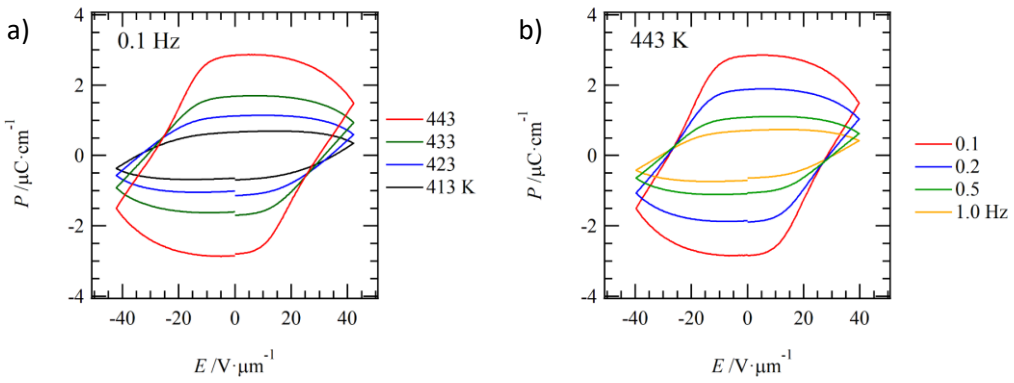

Figure S34. The *P* – *E* hysteresis measurement of **C15TPA** for a) the *T*-dependence at *f* = 0.1 Hz and b) the *f*-dependence at 443 K.

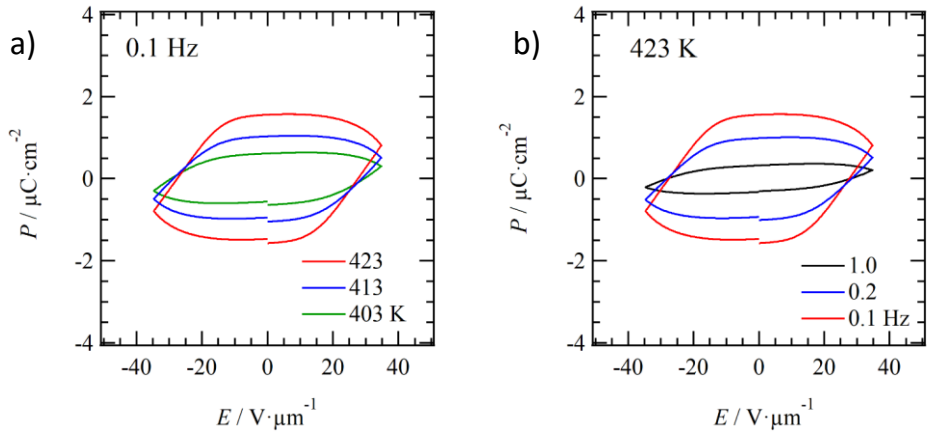

Figure S35. The *P* – *E* hysteresis measurement of **C16TPA** for a) the *T*-dependence at *f* = 0.1 Hz and b) the *f*-dependence at 423 K.

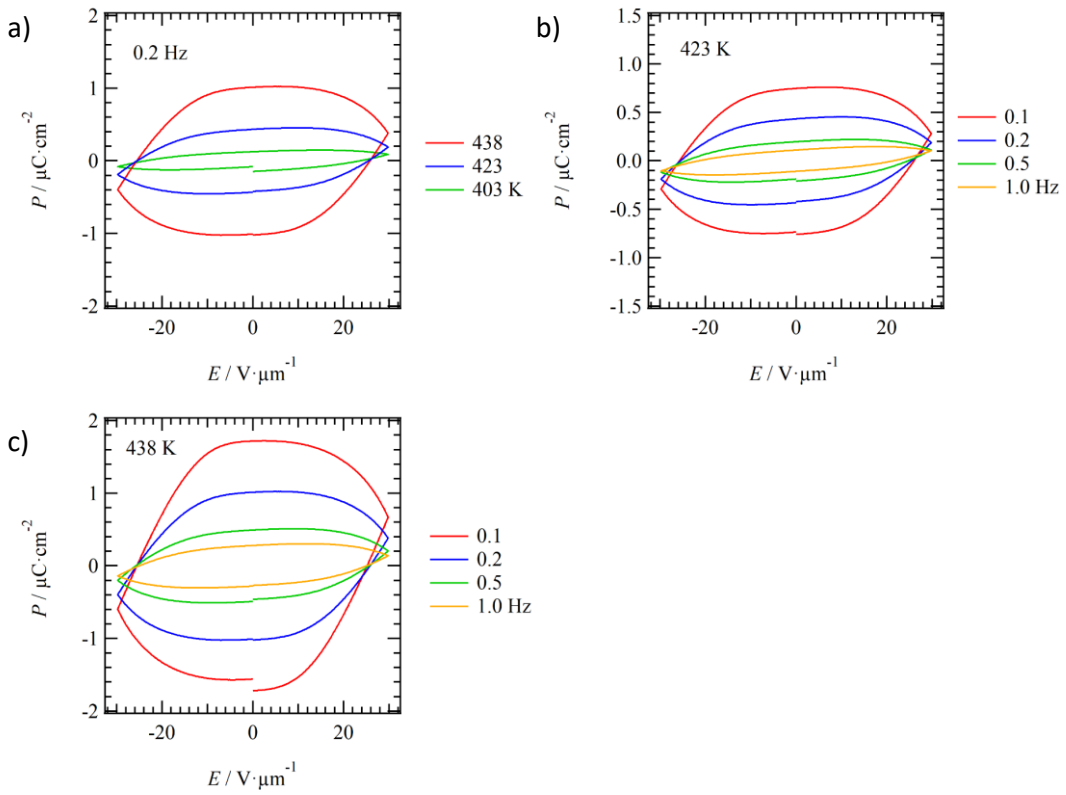

Figure S36. The *P* – *E* hysteresis measurement of **C18TPA** for a) the *T*-dependence at *f* = 0.2 Hz, b) the *f*-dependence at 423 K, and c) the *f*-dependence at 438 K.

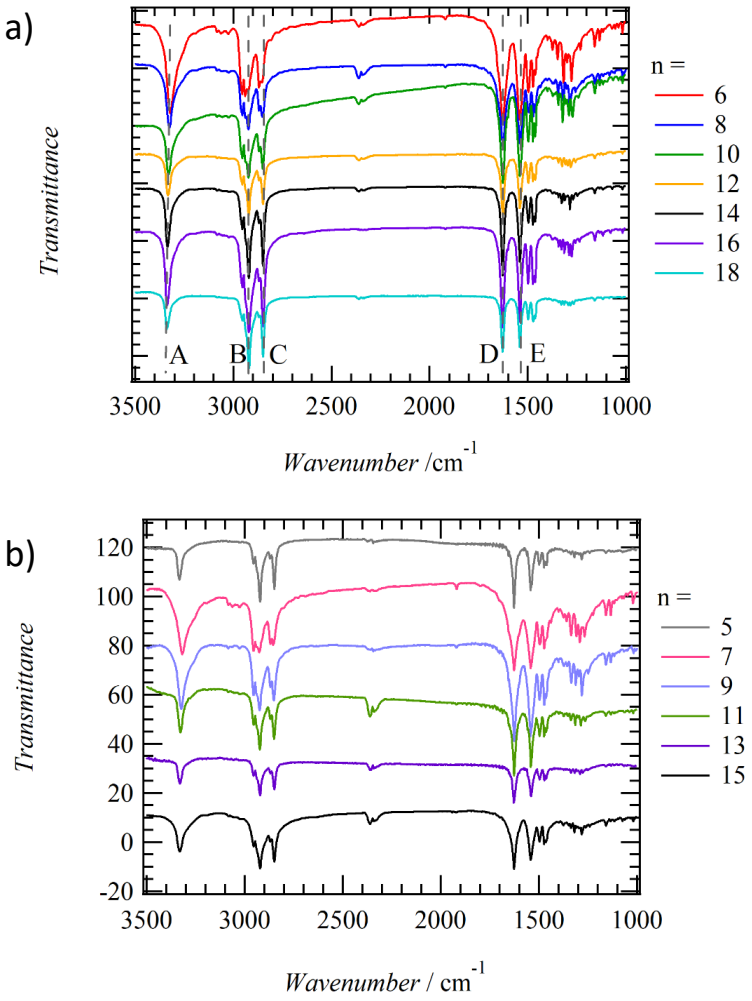

Figure S37. The IR spectra of a) the even-number and b) the odd-number **CnTPAs** at 298 K on KBr pellets.

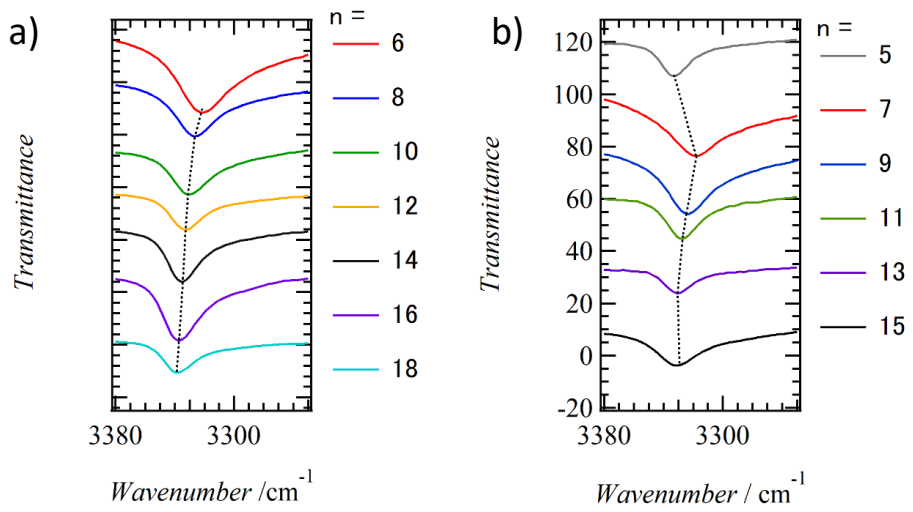

Figure S38. The IR spectra in the energy range 3380 – 3250 cm^{-1} of a) the even-number and b) the odd-number **CnTPAs** at 298 K on KBr pellets.

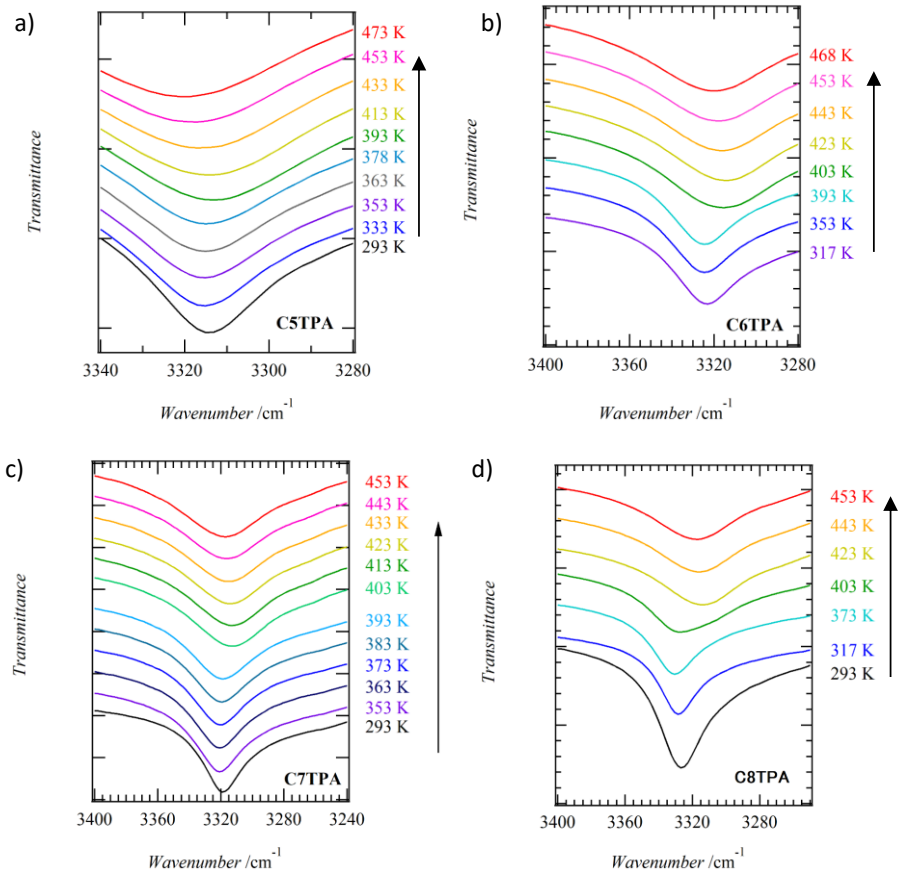

Figure S39. *T*-dependent IR spectra in the energy range 3400 – 3240 cm^{-1} of a) **C5TPA**, b) **C6TPA**, c) **C7TPA**, and **C8TPAs** in the heating process on KBr pellets.

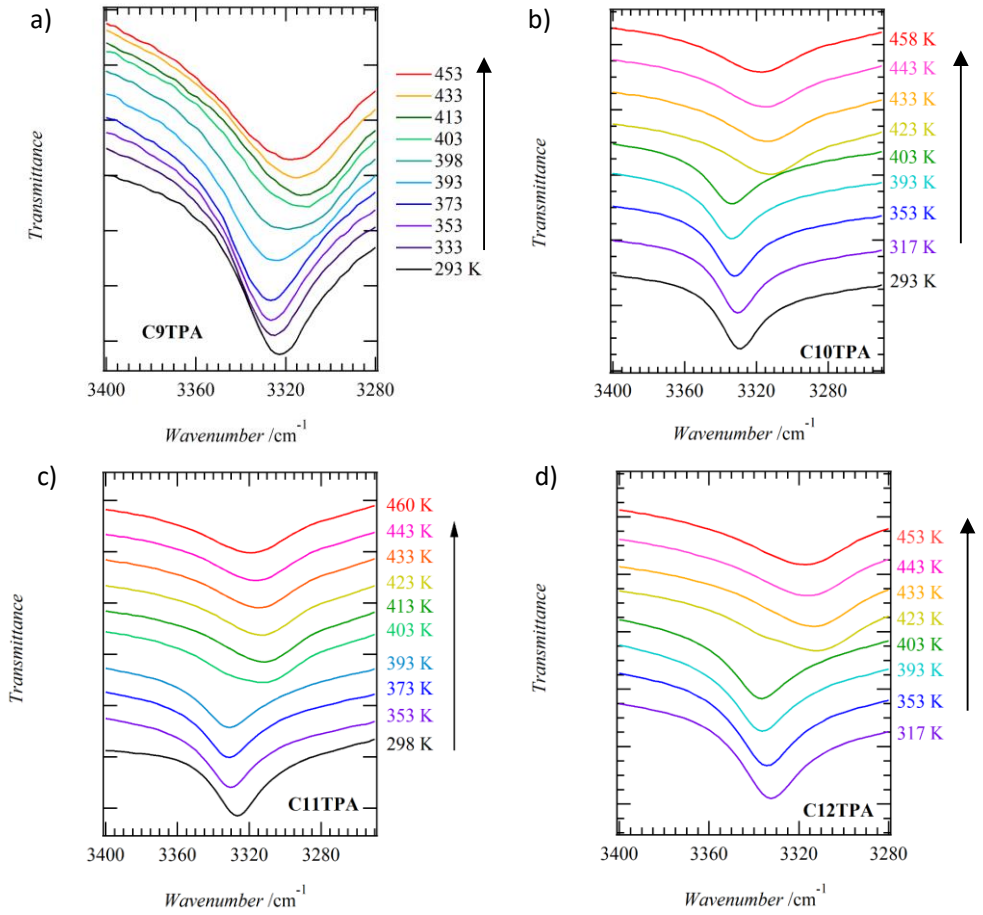

Figure S40. *T*-dependent IR spectra in the energy range 3400 – 3240 cm^{-1} of a) **C9TPA**, b) **C10TPA**, c) **C11TPA**, and **C12TPAs** in the heating process on KBr pellets.

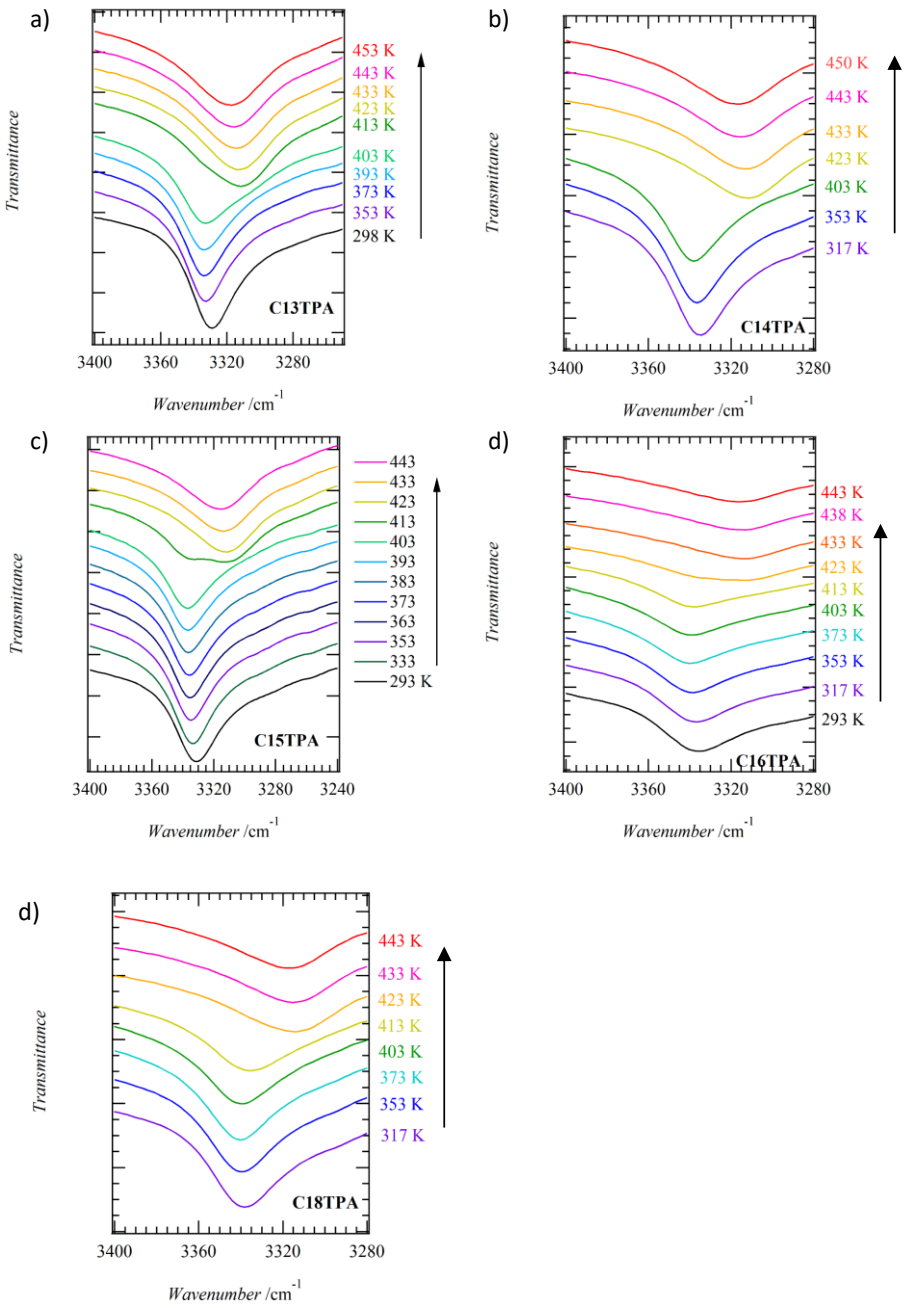

Figure S41. *T*-dependent IR spectra in the energy range 3400 – 3240 cm^{-1} of a) **C13TPA**, b) **C14TPA**, c) **C15TPA**, d) **C16TPA**, and **C18TPAs** in the heating process on KBr pellets.

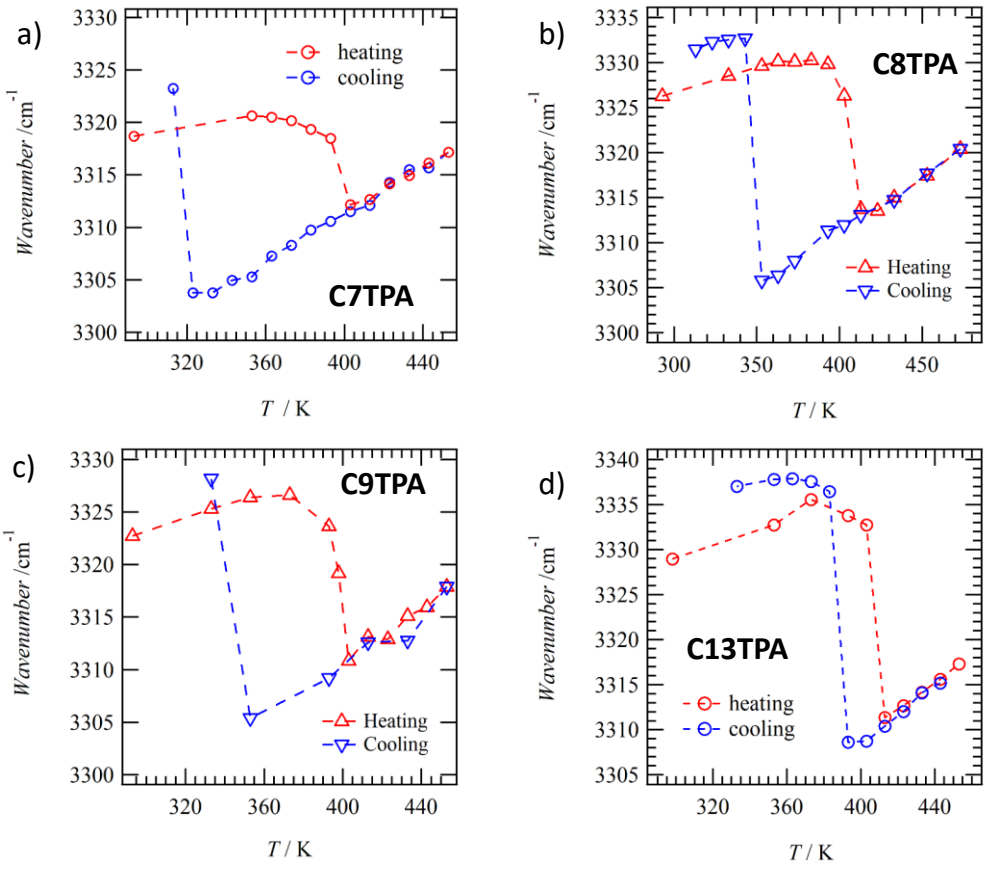

Figure S42. *T*-depedent energy shift of $\nu_{N\text{-}H}$ mode for a) **C7TPA**, b) **C8TPA**, c) **C9TPA**, and **C13TPA**.